# 2-Deoxyglucose dendrimer-enabled niclosamide delivery to FRβ-expressing macrophages alleviates endometriosis progression and associated hyperalgesia

Anubhav Dhull[1#], Mingxin Shi[2#], Madeleine E. Harvey[2#], Taylor M. Page[2], Rishi Sharma[1], Kenneth John Goody[1], Aqib Iqbal Dar[1], Nash S. Moawad[3], Vijay Kumar Sirohi[4], Paul S. Cooke[4], Kanako Hayashi[2]*, Anjali Sharma[1]*

[1]*Department of Chemistry, College of Arts and Sciences, Washington State University, Pullman, WA 99164, USA.*

[2]*School of Molecular Biosciences, Center for Reproductive Biology, Washington State University, Pullman, WA 99164, USA.*

[3]*Department of Obstetrics & Gynecology, University of Florida College of Medicine, P.O. Box 100294, Gainesville, FL 32610, USA.*

[4]*Department of Physiological Sciences, University of Florida, P.O. Box 100144, Gainesville, FL 32611, USA.*

[#]*These authors contributed equally to this work*

*Correspondence:

Anjali Sharma, Department of Chemistry, College of Arts and Sciences, Washington State University, Pullman, WA 99164, USA.

Kanako Hayashi, School of Molecular Biosciences, Center for Reproductive Biology, Washington State University, Pullman, WA 99164, USA.

E-mail: anjali.sharma@wsu.edu, k.hayashi@wsu.edu

***Abstract***

Endometriosis is a chronic, incurable disease. Due to limited efficacy, high recurrence rates, and serious side effects of current treatments, development of new, targeted, non-hormonal therapies is urgently needed. We previously reported that niclosamide, an FDA-approved anthelmintic drug, attenuates endometriotic lesion growth. We further identified folate receptor-β (FRβ)-positive macrophages as contributors to disease progression. Significantly, niclosamide inhibits $FR\beta^+$ macrophages and reduces inflammation, innervation, and angiogenesis. To develop niclosamide as a non-hormonal and selective immune cell-targeted therapy for endometriosis, we engineered a folic acid-conjugated 2-deoxyglucose dendrimer (FA-2DG-D) using click chemistry to enable selective FRβ-mediated uptake. Conjugation of niclosamide to FA-2DG-D yielded a targeted nanotherapeutic (FA-2DG-D-Niclo) with enhanced aqueous solubility, controlled intracellular release, and excellent batch-to-batch reproducibility. In a mouse model of endometriosis, FA-2DG-D demonstrated lesion-specific accumulation and selective internalization by $FR\beta^+$ macrophages with minimal off-target organ retention. A single intraperitoneal dose of FA-2DG-D-Niclo (25 or 50 mg/kg/bw of niclosamide) significantly reduced $FR\beta^+$ macrophage burden, suppressed lesion number and volume, and markedly improved endometriosis-associated hyperalgesia at two weeks post-treatment. Together, these findings establish $FR\beta^+$ macrophages as a potential target in endometriosis and present FA-2DG-D-Niclo as a non-hormonal, macrophage-focused nanomedicine for precise and effective endometriosis treatment.

**Keywords**: endometriosis, niclosamide, dendrimer, macrophages, non-hormonal therapy

## Graphic Abstract

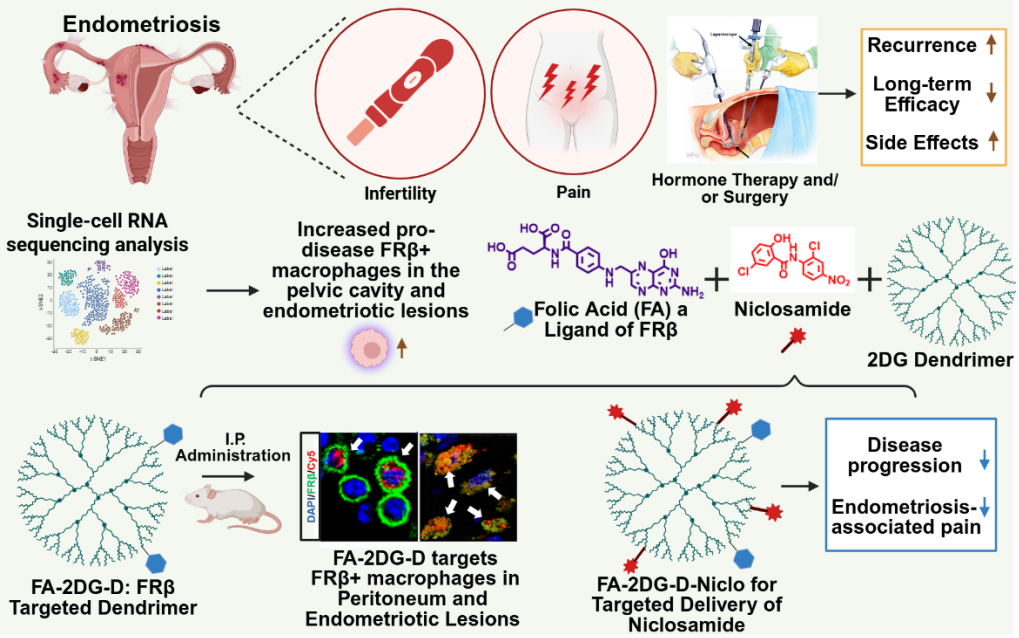


*Created via Biorender.com*

## 1. Introduction

Endometriosis affects an estimated 10% of reproductive-aged women, roughly 190 million individuals worldwide, and remains one of the most debilitating gynecological disorders [1]. The disease is characterized by chronic pelvic pain, dysmenorrhea, dyspareunia, and infertility, all of which severely diminish the quality of life for patients and their families [2-4]. In the United States alone, the annual economic burden is estimated at $78-119 billion, encompassing healthcare costs, productivity losses, and reduced workforce participation [5]. Despite its prevalence and impact, endometriosis remains incurable, and the therapeutic landscape has changed little over the past several decades. Current medical management relies on hormonal suppression of estrogen production or action [6, 7], such as oral contraceptives, progestins, and/or gonadotropin-releasing hormone (GnRH) agonists/antagonists [6, 8], as well as surgical excision of lesions. However, hormonal treatments are limited in efficacy, have high recurrence rates, and cause significant side effects. Surgical excision offers temporary relief of symptoms, yet nearly half of surgically treated women experience recurrence within five years, and ~12% fail to achieve meaningful pain reduction after surgery [9, 10]. Thus, there is an urgent need to identify new therapeutic targets to develop novel non-hormonal treatments in endometriosis.

A growing body of evidence implicates immune dysfunction, particularly macrophage dysregulation, in driving lesion establishment, chronic inflammation, angiogenesis, and neurogenesis in endometriosis [11-13]. Recently, our single-cell transcriptomic analysis identified a unique FRβ-expressing macrophage population, differentiated from monocyte-derived proinflammatory macrophages and characterized by residential macrophage traits in mouse endometriosis [14]. The population of macrophages is also identified in the lesions of endometriosis patients [15]. The selective upregulation of $FR\beta^+$ on these macrophages can be used as an accessible and disease-restricted cellular target for ligand-guided targeted drug delivery.

Our prior studies demonstrated that niclosamide significantly suppressed endometriotic lesion growth, alleviated aberrant peritoneal inflammation, and decreased vascularization and innervation in lesions using two distinct mouse models of endometriosis without compromising fertility [13, 14, 16]. Niclosamide (5-chloro-*N*-(2-chloro-4-nitrophenyl)-2-hydroxybenzamide) is a chlorinated salicylanilide derivative that is FDA-approved as an anthelmintic drug. Currently, multiple clinical trials are ongoing to repurpose it for the treatment of other diseases, including cancer and metabolic diseases [17]. However, the clinical use of niclosamide is significantly

limited by its poor aqueous solubility and correspondingly low oral bioavailability. To address these challenges, researchers are actively developing innovative formulation strategies such as water-soluble derivatives, solid dispersions, and nanocarrier-based delivery systems to enhance its solubility, pharmacokinetics and overall therapeutic potential [18]. Additionally, systemic niclosamide treatment inhibits several pathways, including STAT3, NFκB, and WNT signaling, across all cell types [11, 12, 16], including other macrophages [14]. Disrupting these essential pathways across all cell types would lead to unwanted side effects and this poses a significant barrier to therapeutic use of niclosamide. Importantly, niclosamide can also reduce elevated FRβ$^+$ macrophages and restore the perturbed microenvironment in endometriosis by finely regulating macrophage dynamics [14], suggesting that FRβ$^+$ macrophages can serve as a viable therapeutic target in endometriosis. Therefore, targeted delivery of niclosamide to FRβ$^+$ macrophages offers a strategy to maximize therapeutic efficacy while minimizing systemic toxicity.

In this context, dendrimer nanotechnology has emerged as a powerful tool for targeted therapeutic delivery, enabling selective engagement of pathogenic cells while minimizing off-target toxicity [19-24]. Dendrimers are monodisperse, highly branched macromolecules whose multivalent surface architecture and tunable chemistry allow precise conjugation of targeting ligands, therapeutic agents, and imaging probes [25-27]. Building on our previously synthesized 2-deoxy-glucose (2DG) functionalized dendrimer (2DG-D) [28], which incorporates 2DG moieties to enhance solubility and macrophage interaction, we engineered a folic acid (FA), a ligand of FRβ, conjugated dendrimer (FA-2DG-D) by covalently coupling FA to the dendrimer surface through orthogonal click chemistry. This design exploits ligand-FRβ binding to selectively direct dendrimer uptake into FRβ$^+$ macrophages within endometriotic lesions and peritoneum [29, 30]. To achieve targeted delivery, we further developed the niclosamide conjugated FA-2DG-D (FA-2DG-D-Niclo). Here, we report the design, synthesis, and in vivo evaluation of FA-2DG-D and FA-2DG-D-Niclo in a mouse model of endometriosis. Our results demonstrate that FA-2DG-D has FRβ$^+$ macrophage-specific targeting in the lesions and peritoneum and delivers niclosamide into FRβ$^+$ macrophages with ligand-receptor internalization. This targeted dendrimer platform offers a promising strategy for therapeutic delivery in endometriosis, addressing a critical unmet need for more precise and effective interventions.

## 2. Methods

114 ***2.1. Human Sample Collection***

115 All procedures involving human subjects were performed in accordance with ethical
116 approval by the Institutional Review Board (IRB) guidelines for the University of Florida under
117 IRB code NO. IRB202003131. All patients were recruited from the Division of Minimally Invasive
118 Gynecologic Surgery of the University of Florida Health Shands Hospital, Gainesville, Florida.
119 Participants were either previously diagnosed with endometriosis or suspected of having
120 endometriosis, with symptoms including ovarian cysts, chronic pelvic pain, dysmenorrhea,
121 dyschezia, dyspareunia, uterine bleeding, and myofascial pain syndrome. Endometriosis is further
122 confirmed by pathological analysis of the excised lesions obtained during surgery. Informed
123 written consent was obtained from each participant before the procedure. In this study, peritoneal
124 washings from 4 patients aged 19 to 37 years (**Supplementary Table S1**) were collected at the
125 beginning of the procedure. Briefly, the pelvic cavity was irrigated using approximately 100 mL
126 of sterile saline, and approximately 80 mL of peritoneal washings containing pelvic exudate cells
127 were collected from each patient and placed on ice immediately. Red blood cells were removed by
128 resuspending cells with 500 μL Red Blood Cell Lysis Buffer (BioLegend, Cat.#420301). Cells
129 were then counted and cryopreserved with freezing media containing 90% fetal bovine serum
130 (FBS) and 10% dimethyl sulfoxide, and stored at −80 °C for further analysis.

131

132 ***2.2. Single-cell RNA-Sequencing and Analysis***

133 ***2.2.1. Library Preparation and Sequencing***

134 To perform single-cell RNA sequencing (scRNA-seq), frozen pelvic exudate cells were
135 thawed in a 37 °C water bath and prepared following the 10x Genomics protocol named "Fresh
136 frozen human peripheral blood mononuclear cells for single-cell RNA sequencing" (document
137 #CG00039 Rev E). Briefly, thawed cells were slowly transferred into a 50 mL conical tube and
138 recovered by sequential 1:1 dilution with warmed FBS for a total of 5 times. Cell viability was
139 assessed to ensure samples with viability greater than 80%. After centrifuging at 300g for 5 min
140 at room temperature, the cells were resuspended in phosphate-buffered saline (PBS) with 0.04%
141 bovine serum albumin (BSA) at a concentration of 900-1,200 cells/μl. Cells were then placed on
142 ice and immediately proceeded to library construction using a 10x Genomics Chromium Next
143 GEM Single Cell 3' Kit v3.1, following the standard kit user guide (document #CG000204) for a
144 target of 6000 cells. Libraries were sequenced on Illumina NovaSeq 6000. FASTQ files were

aligned to the human reference genome GRCh38 via Cell Ranger v7.1.0 [31], and an average of 107,903 reads per cell was achieved for each RNA library (**Supplementary Table S2**).

### *2.2.2. External Human Endometrial and Pelvic Exudate Cell scRNA-seq Datasets*

We integrated publicly available human scRNA-seq datasets from eutopic endometrium with or without endometriosis, ectopic endometrium, and pelvic exudate cells. Processed Cell Ranger output files or raw FASTQ files were downloaded from the Gene Expression Omnibus (GEO), ArrayExpress, or the Sequence Read Archive (SRA). These datasets included: (1) Wang et al. (GSE111976) [32], (2) Lai et al. (GSE183837) [33], (3) Garcia-Alonso et al. (E-MTAB-10287) [34], (4) Tan et al. (GSE179640) [15], (5) Fonseca et al. (GSE213216) [35], (6) Huang et al. (GSE214411) [36], (7) Marečková et al. (E-MTAB-14039) [37], (8) Shin et al. (PRJNA932195) [38], (9) Han et al. (GSE228030) [39], and (10) Zou et al. (PRJNA713993) [40], as shown in **Figure 1A and B**. For all datasets, only samples collected from women of reproductive age were included. For endometrial scRNA-seq datasets from (1) to (8), patients labeled as undergoing hormonal treatments during sample collection were also excluded. Samples used in this study are summarized in **Supplementary Table S3**.

### *2.2.3. Single-cell Data Pre-processing and Clustering*

RNA matrices from both newly generated and existing public datasets were individually imported to Scanpy v.1.8.1 for further analysis [41]. Low-quality cells were excluded using the following criteria: (1) genes that were detected in fewer than 3 cells, (2) cells with fewer than 300 genes, (3) a maximum of 100,000 UMIs, and (4) a maximum of 20% mitochondrial content. Doublets were detected and removed using Scrublet [42]. Filtered matrices from endometrial or pelvic cell scRNA-seq datasets were combined separately and analyzed independently. For each combined endometrial or pelvic cell scRNA-seq matrix, gene expression values were normalized with a global scaling factor of 10, 000 and log-transformed. Top 3,000, or 2,000 highly variable genes for the endometrial, or pelvic cell datasets, respectively, were identified by Scanpy. The mitochondrial genes, haemoglobin genes, and ribosomal genes were excluded from the highly variable gene set [43]. Principal component analysis (PCA) was performed using the highly variable gene set. After Harmony (v.0.0.10) [44] batch effect correction, harmony-corrected components were used to generate the neighborhood graph and perform dimensionality reduction

using uniform manifold approximation and projection (UMAP). The Leiden algorithm was then used for clustering analysis [45]. Marker genes of each cluster were identified using the Wilcoxon rank-sum test [46] with the default setting (**Supplementary Table S4**). Major cell types were determined by manually annotating cell clusters with previously established marker genes from the literature [15, 39, 47, 48].

#### *2.2.4. Identification of Enriched Genes and Gene Ontology Analysis in FOLR2$^+$ Endometrial and Pelvic Cells*

To understand the transcriptional profiles of folate receptor beta-positive (FOLR2$^+$) macrophages, cells with specific FOLR2 expression (FOLR2>0) were labeled and extracted from endometrial and pelvic cell matrices. Enriched genes in FOLR2$^+$ cells were identified by the Wilcoxon rank-sum test in a one-versus-rest fashion, with a minimum $\log_2$(fold change) of 2 (**Supplementary Table S5**). Gene Ontology (GO) was performed on the identified enriched genes in FOLR2$^+$ endometrial or pelvic cells using clusterProfiler (v.4.2.2) [49]. The enriched GO list was further filtered with the *simplify* function (cutoff = 0.7) to remove redundant terms (**Supplementary Table S6**). Differentially expressed genes (DEGs) among eutopic endometrium without (Control; Cont) or with endometriosis (EuE), and ectopic endometrium (EcE) in the endometrial FOLR2$^+$ macrophages, and DEGs between control (Cont) and endometriotic (Endo) pelvic exudate cells, were identified by Wilcoxon rank-sum test, with a minimum $\log_2$(fold change) of 0.5 (**Supplementary Table S7**).

### *2.3. Chemistry Experimental Section*

Experimental methods related to materials, instrumentation, synthesis protocols, characterization of compounds (**Supplementary Figures S1-S15 and S17-S34**), in vitro drug release studies, and FA-2DG-D-Niclo formulation stability studies are presented in the **Supplementary Information**.

### *2.4. Animals*

C57BL/6 mice were purchased from Inotiv and housed in an environment-controlled animal facility (20-22 °C, ~40% relative humidity, and 12:12 light-dark cycle) with *ad libitum*

206 access to food and water. All animal experiments were conducted at Washington State University
207 in accordance with NIH guidelines for care and use of laboratory animals (protocol #6751).
208
209 ***2.5. Mouse Model of Endometriosis***
210 An experimental mouse model of endometriosis was employed, using procedures
211 previously described and adopted by us, with minor modifications [50]. Briefly, to induce
212 endometriosis-like lesions (ELL), female donor mice were injected subcutaneously with pregnant
213 mare serum gonadotropin (PMSG; 5 IU; Sigma, St. Louis, MO) to stimulate an estrogenic response
214 within the uterus. Uteri were harvested from these donors 41 hours after PMSG injection. The
215 endometrium was then scraped from myometrium and dissected into fragments (1-2 mm per side),
216 and introduced as the source of syngeneic mouse endometrium (50 mg of fragments) via injection
217 (in 0.2 mL of PBS) into the peritoneal cavity in the ovary-intact recipient females under anesthesia
218 via inhaled isoflurane.
219
220 ***2.6. Animal Study Design***
221 ***2.6.1. In Vivo Dendrimer Biodistribution***
222 Adult female mice (n=36, ~3 months old) were randomly divided into three groups
223 (n=3/group/timepoint): 1) sham controls administered with Cy5-labeled dendrimer FA-2DG-D-
224 Cy5; 2) ELL-induced mice administered with 2DG-D-Cy5; 3) ELL-induced mice administered
225 with FA-2DG-D-Cy5. The animals in the ELL groups received donor endometrium to induce
226 endometriotic lesions, and the sham control mice received PBS. One week following lesion
227 induction, all mice received FA-2DG-D-Cy5 or 2DG-D-Cy5 injected into the tail vein, as listed in
228 the above group description, at a dose of 50 mg/kg (300 μL). Mice were then euthanized at 1, 6,
229 24, and 72 hours after injection. The whole skin was gently peeled off to acquire the whole-body
230 Cy5 fluorescence distribution using an in vivo imaging system (IVIS; Revvity). Lesions and/or
231 major organs, including the brain, heart, spleen, lungs, liver and kidneys, were dissected to obtain
232 ex vivo fluorescence images and stored at -80 °C. The fluorescence intensity of the region of
233 interest (ROI) was calculated with the Living Image software (4.7.4) accompanying IVIS.
234 Amounts of dendrimer in major organs and lesions were further examined ex vivo using
235 fluorescence intensity-based quantification.
236

237 ***2.6.2. Ex Vivo Dendrimer Quantification***

238 Frozen organs (lesions, liver, spleen, heart, kidneys, brain and lungs) were slowly thawed
239 on ice and weighed. Tissue samples were then dissected to obtain known masses from each organ.
240 Samples were homogenized in methanol (1 mL per 100 mg tissue) with stainless steel beads using
241 a tissue homogenizer. The homogenized samples were centrifuged at 4°C, and the clear
242 supernatants were transferred to protein LoBind Eppendorf tubes and stored at -80°C. For
243 fluorescence quantification, thawed supernatants were centrifuged again before analysis.
244 Fluorescence intensity was measured on a Varioskan Lux Multimode Microplate Reader
245 (ThermoFisher), using λ_ex = 650 nm and λ_em = 670 nm for Cy5. Background fluorescence from
246 control solvent was subtracted, and corrected fluorescence values were converted to 2DG-D-Cy5
247 and FA-2DG-D-Cy5 concentrations using calibration curves generated at 5-10 slit widths.
248

249 ***2.6.3. In Vivo Cellular Uptake of Dendrimer***

250 To evaluate the specificity of cellular uptake of the dendrimer, endometriotic lesions were
251 induced in 6 female mice. On Day 7 following lesion induction, mice received an intraperitoneal
252 (i.p.) injection of FA-2DG-D-Cy5 or 2DG-D-Cy5 (50 mg/kg/bw, n=3/group). Peritoneal cells,
253 lesions, kidney, liver and spleen were collected at 2 weeks after dendrimer injection. Specific
254 cellular uptake of the dendrimer was then assessed by immunostaining.
255

256 ***2.6.4. In Vivo Efficacy of Dendrimer-Niclosamide***

257 The efficacy of targeted delivery of niclosamide with FA-conjugated dendrimer (FA-2DG-
258 D-Niclo) was examined using the mouse model of endometriosis described above. On Day 7, ELL-
259 induced mice were administered a single i.p. injection of control (FA-2DG-D), or 25 mg or 50
260 mg/kg body weight (bw) of FA-2DG-D-Niclo. Behavioral tests were performed on Day -1 (a day
261 before lesion induction), Day 7 (before dosing), and Day 14 or 21 (1 or 2 weeks after dosing, n=16
262 at Day -1 and Day 7, n=8 at Day 14 and Day 21). Mice were then euthanized on Day 14 or 21 after
263 the last behavioral test. Peritoneal fluid was recovered by lavage (4 mL x 2 of ice-cold PBS with
264 3% FBS) for immune profiling. The number and volume of lesions were recorded. Lesions were
265 fixed in 4% paraformaldehyde for further analysis.
266

267 ***2.7. von Frey Test***

268 A standard behavioral (mechanical sensitivity) test was performed before sample
269 collection, as described by our laboratory previously [51, 52]. Mice (n=8/group/time point) were
270 allowed to acclimate quietly in the testing room for 30 minutes under red light. Then, von Frey
271 filaments (BIO-VF-M, Bioseb) were applied 10 times to the skin perpendicular to the lower
272 abdomen and bilateral hind paws to evaluate local or systemic sensitivity, respectively. The force
273 in grams (g) of the filament evoking a withdrawal response (50% response count as sensitive) was
274 recorded. Three behaviors were considered positive responses to filament stimulation: 1) sharp
275 retraction of the abdomen, 2) immediate licking and/or scratching of the area of filament
276 stimulation, or 3) jumping. All behavioral tests were performed with investigators blinded to
277 treatment groups. These data were then subsequently analyzed by another blinded investigator.
278
279 ***2.8. Flow Cytometry***
280 Single-cell suspensions of peritoneal exudate cells were used for immune cell profiling by
281 flow cytometry as described previously [51, 52]. Briefly, peritoneal exudate cells were lysed using
282 Red Blood Cell Lysis Buffer (BioLegend) and incubated at room temperature for 20 minutes with
283 Zombie Aqua™ Fixable Viability dye (BioLegend). Cells were blocked on ice for 20 minutes with
284 Fc Block anti-CD16/CD32 (ThermoFisher) and stained with fluorochrome-conjugated
285 monoclonal antibodies for 1 hour (**Supplementary Table S8**). Samples (n=8/group) were acquired
286 with the Attune NxT Acoustic Focusing Cytometer using Attune NxT software (ThermoFisher),
287 and data were analyzed with FlowJo v10.4 software (FLOWJO).
288
289 ***2.9. Immunohistochemistry and Confocal Imaging***
290 The peritoneal exudate cell suspension was first fixed with 4% paraformaldehyde at RT for
291 15 min, and blocked with 10% donkey serum at RT for 30 min. Cells were then incubated with
292 FRβ primary antibody (1:200, Abcam, Cat.#ab302532) at 4°C overnight and AlexaFluor 488-
293 conjugated F(ab') secondary antibody (Molecular Probe) at RT for 1 hour. Following DAPI
294 staining, the cells were resuspended with Fluoromount-G (SouthernBiotech) and mounted on
295 slides. The mounted slides were imaged using a Leica SP8-X Confocal Microscope.

296 Immunohistochemistry of FRβ on cross-sections (5 μm) of paraffin-embedded tissues,
297 including lesion, kidney, and liver, was performed using the FRβ primary antibody (1:400) and
298 AlexaFluor 488-conjugated F(ab') secondary antibody, or VECTASTAIN ABC kit (Vector Lab).

299 Immunostaining images were acquired by Leica SP8-X Confocal Microscope or Leica DM4 B
300 microscopy. FRβ-positive cells in lesions were counted by Image J in an area of 0.07244 $mm^2$, and
301 the number of $FR\beta^+$ cells per 1 $mm^2$ was shown.

302

303 ***2.10. Statistical Analysis***

304 Statistical analyses were performed using GraphPad Prism (version 9.5). To compare
305 differences in dendrimer organ uptake among groups, one-way ANOVA followed by the Tukey
306 multiple comparison tests was used. To analyze behavioral test results, time-dependent differences
307 within a single group were compared using one-way ANOVA followed by the Dunnett's multiple-
308 comparison test. To compare effects of different niclosamide dosages of niclosamide at each time
309 point, one-way ANOVA was used with Tukey multiple comparison tests. Differences in lesion
310 number, volume, and $FR\beta^+$ or $CD45^+$ cell counts between groups at each time point were analyzed
311 using one-way ANOVA followed by the Tukey multiple-comparison test. In all cases, data were
312 tested for normal distribution using the Shapiro-Wilk normality test. If data were normally
313 distributed, one-way ANOVA was used to analyze differences among groups. If data were not
314 normally distributed, the Kruskal-Wallis test was performed, as stated in the figure caption.
315 Significance was defined as $p < 0.05$ (*), $p < 0.01$ (**), $p < 0.001$ (***), or $p < 0.0001$ (****).

316

317 **3. Results and Discussion**

318 ***3.1. FRβ-expressing Macrophages in Eutopic and Ectopic Endometrium, and Pelvic Exudate***
319 ***Cells in Endometriosis***

320 We performed an integrated analysis with our newly generated pelvic exudate cell scRNA-
321 seq dataset from women with endometriosis (**Supplementary Tables S1 and S2**), along with
322 publicly available human datasets, including eutopic endometrium without or with endometriosis,
323 ectopic endometrium (lesion), and pelvic exudate cells (**Figure 1A-B, Supplementary Table S3**).
324 After data merging and quality control filtering, 748,509, and 76,187 total high-quality endometrial
325 and pelvic exudate cells were retained, respectively. Clustering analysis identified 7 major cell
326 types in the endometrium (EM), including B lymphocytes ($CD79A^+$), endothelial cells
327 ($PECAM1^+$), epithelial cells ($EPCAM^+$), myeloid cells ($LYZ^+$), perivascular cells ($RGS5^+$),
328 stromal cells ($DCN^+$), and T lymphocytes and natural killer (NK) cells ($CD3E^+$ and $CD2^+$) (**Figure**
329 **1C and E, Supplementary Table S4**). In the pelvic cavity (P), B lymphocytes ($CD79A^+$),

330 dendritic cells ($CD1C^+$), macrophages (Mac, $CD14^+$), mast cells ($TPSAB1^+$), NK cells ($GNLY^+$),
331 and T lymphocytes ($CD3D^+$) were assigned as overarching cell types (**Figure 1D and F,**
332 **Supplementary Table S4**). As expected, UMAP projection confirmed that $FOLR2^+$ cells are
333 localized within the myeloid cell clusters of endometrial and pelvic exudate cells (**Figure 1G-H**).
334 Gene Ontology (GO) enrichment analysis indicated that both endometrial and pelvic $FOLR2^+$
335 macrophages were primarily associated with myeloid migration and activation and immune
336 regulation (**Figure 1I-J, Supplementary Table S6**). In particular, biological processes associated
337 with cytokine production, leukocyte cell-cell adhesion, and interleukin-6 (IL-6) production were
338 predominantly enriched in the $FOLR2^+$ macrophages of the endometrium. Stronger association
339 with phagocytosis, cholesterol regulation, and response to bacteria was detected in the pelvic
340 $FOLR2^+$ macrophages, consistent with the primary roles of residential $FOLR2^+$ macrophages in
341 host defense and metabolic processes [53-55]. Comparative analysis showed a significantly higher
342 abundance of $FOLR2^+$ macrophages in ectopic endometrium (EcE) than in eutopic endometrium
343 with (EuE) and without (Cont) endometriosis (**Figure 1K**). Similarly, in pelvic exudate cells,
344 significantly elevated numbers of $FOLR2^+$ macrophages were observed in patients with
345 endometriosis (**Figure 1L**). Furthermore, DEG analysis of endometrial and pelvic $FOLR2^+$
346 macrophages demonstrated that significant upregulation of proinflammatory (CCL2, IL-6R, and
347 NFKB1), angiogenesis (FGFR1, HIF1A, and MMP2), and adhesion-related genes (ITGAV,
348 TGFBR1, and TGFBR2) in endometriosis-associated endometrium (EuE and/or EcE) and pelvic
349 cells (Endo) (**Figure 1M-N, Supplementary Table S7**). Collectively, these results indicate an
350 expansion of a pro-disease $FOLR2^+$ macrophage subpopulation in the ectopic endometrium and
351 pelvic cavity in endometriosis patients with pro-disease functions.
352
353 ***3.2. Synthesis and Characterization of FA-2DG-D Using Click Chemistry***
354 A major challenge in developing nanomaterial-based drug delivery systems lies in the
355 complexity and limited reproducibility of synthetic procedures, scalability constraints, and poor
356 batch-to-batch consistency. To overcome these limitations, we used efficient copper(I) catalyzed
357 alkyne-azide cycloaddition (CuAAC) click reaction to design and synthesize the FA-2DG-D
358 conjugate capable of selectively targeting $FR\beta^+$ macrophages for treating endometriosis. This click
359 chemistry-based approach offers a robust and versatile strategy for achieving precise, reproducible,

360 and site-specific conjugation of targeting ligands or therapeutic molecules to polymeric
361 nanocarriers, including dendrimers [28, 56-58].

362 Folic acid (**1**) was functionalized with an azide group to enable its participation in the
363 CuAAC reaction. The folate receptor recognizes folic acid through its pterin and *p*-aminobenzoate
364 moieties via multiple hydrogen bonds and electrostatic interactions within the receptor pocket [59].
365 To preserve these recognition elements, conjugation with the azide linker was performed through
366 the α-carboxylic acid group of the glutamic acid residue, forming a stable amide linkage with the
367 terminal amine of the linker. The carboxylic acid in the ligand was activated using
368 dicyclohexylcarbodiimide (DCC) and *N*-Hydroxysuccinimide (NHS), and the resulting NHS-
369 activated intermediate was reacted with azido-PEG5-amine (**2**) in the presence of DIPEA to yield
370 the desired FA-Azide (**3**). Successful formation of the azide-functionalized folic acid was
371 confirmed by $^{1}$H NMR spectroscopy, which showed characteristic PEG proton signals from the
372 azide linker at δ 3.0 (2H), 3.4 (2H), and 3.5-3.7 (20H) ppm, along with a new amide proton signal
373 at δ 7.3 ppm (**Figures 2B and Supplementary Figure S1**). HPLC analysis confirmed the purity
374 of the product, exhibiting a single peak with a retention time of 13.3 minutes with more than 98%
375 purity (**Supplementary Figure S3**). To enable the subsequent CuAAC coupling, terminal alkyne
376 groups were introduced on the surface of 2DG-D. The primary hydroxyl groups of the surface-
377 exposed 2DG moieties were utilized for this modification. 2DG-D (**4**) was reacted with 5-hexynoic
378 acid (**5**) in the presence of 1-ethyl-3-(3-dimethylaminopropyl)carbodiimide hydrochloride (EDC)
379 and 4-(dimethylamino)pyridine (DMAP) to afford 2DG-D-Hexyne (**6**) (**Figure 2A**). $^{1}$H NMR
380 spectrum showed new methylene proton signals from the hexynoic linker in the aliphatic region at
381 δ 1.75-1.68 (8H), 2.46-2.34, and 2.74-2.58 (8H) ppm (**Figures 2B and Supplementary Figure**
382 **S5**), confirming the attachment of 4 hexyne arms. HPLC analysis showed a shift in retention time
383 from 14.0 minutes for 2DG-D (**4**) to 19.7 minutes for 2DG-D-Hexyne (**6**), confirming successful
384 surface modification (**Supplementary Figures S7 and S15**). Finally, the CuAAC reaction
385 between FA-Azide (**3**) and 2DG-D-Hexyne (**6**) yielded the FRβ$^{+}$ macrophage-targeted platform
386 FA-2DG-D (**7**). Previous studies have demonstrated that dendrimers bearing a single folic acid
387 ligand exhibit monovalent, reversible binding with folate-binding protein (FBP), whereas
388 dendrimers conjugated with two or more folic acid molecules engage in multivalent interactions,
389 resulting in stronger receptor binding [60-62]. Given the high hydrophobicity of folic acid,
390 conjugating more than 2 ligand molecules could potentially reduce the dendrimer's aqueous

solubility. Our CuAAC click chemistry approach ensured desired loading of folic acid on the dendrimer. The number of attached molecules was confirmed through the comparative integration of aromatic protons from the dendrimer at δ7.2 ppm (16H), and the aromatic and amide protons of folic acid at δ8.7 ppm (2H), 7.7 ppm (4H), 7.0 ppm (4H) and at 6.7 ppm (4H). The HPLC chromatogram showed a retention time shift from 19.7 minutes for 2DG-D-Hexyne (**6**) to 16.1 minutes for FA-2DG-D (**7**) (**Supplementary Figures S7** and **S10)**. The purity of FA-2DG-D (**7**) was determined to be more than 96% by HPLC (**Supplementary Figure S10**). Dynamic light scattering (DLS) analysis revealed a hydrodynamic diameter of 6.6 ± 0.4 nm and a zeta potential of –5.8 ± 0.3 mV (**Supplementary Figures S11 and S12**).

To enable visualization and assessment of uptake of the dendrimer in FRβ$^+$ macrophages in endometriosis, the dendrimer was further functionalized with a near-infrared dye, cyanine 5 (Cy5). The FA-2DG-D **(7)** containing approximately two terminal alkynes on its surface was conjugated with Cy5-azide (**8**) via a CuAAC reaction, yielding the fluorescently labeled FA-2DG-D-Cy5 (**9**). Successful conjugation was confirmed by the appearance of characteristic Cy5 proton signals in the $^1$H NMR spectrum (**Figure 2B**). The number of Cy5 molecules attached to the dendrimer surface was estimated by proton integration. Comparison of the dendrimer aromatic protons at δ 7.2 ppm (16H) with the Cy5 aromatic protons at δ 8.4 (4H), 8.2 (4H), 7.4 (4H), 6.6 (2H), and 6.4 ppm (2H) indicated the attachment of approximately two Cy5 molecules (**Figures 2B and Supplementary Figure S13**). The HPLC chromatogram of FA-2DG-D-Cy5 (**9**) exhibited a retention time shift from 16.1 to 17.7 minutes following Cy5 conjugation, with a purity exceeding 97% (**Supplementary Figures S14** and **S15**). In addition, the Cy5-labeled dendrimer displayed a characteristic UV absorbance at 650 nm, corresponding to Cy5, which further confirmed successful conjugation. A Cy5-labeled 2DG-D dendrimer (2DG-D-Cy5), lacking the folic acid targeting ligand, was prepared as a non-targeted control for uptake studies following our previously reported procedure [27].

### *3.3. Fluorescence Imaging and Quantitative Analysis of the Biodistribution of Systemically Administered 2DG-D-Cy5 and FA-2DG-D-Cy5 in a Mouse Model of Endometriosis*

We first evaluated the selective FRβ$^+$ macrophages targeting capability of FA-2DG-D-Cy5 in ELL-induced mice at 1, 6, 24, and 72 hours (n=3) and compared it with sham controls (n=3).

To evaluate the contribution of folic acid (FA) toward lesion targeting, biodistribution studies of non-targeted 2DG-D-Cy5 in ELL-induced mice (n=3) were also performed under identical conditions (**Figure 3**). One week after lesion induction, 50 mg/kg bw of fluorescently labeled (FA-2DG-D-Cy5) or non-targeted (2DG-D-Cy5) was injected into the tail vein. Cy5 fluorescent signals were calculated via the IVIS system at 1, 6, 24, and 72 hours. FR$\beta^+$ macrophages in the lesions showed a pronounced elevation in fluorescent (Cy5) signal starting at 1 hour post-injection (green arrows), which persisted above that of the 2DG-D-Cy5 group over the 72-hour observation period (**Figure 3A**). The ex vivo fluorescent results at 72 hours showed specific uptake of FA-2DG-D-Cy5 in the lesion, although some nonspecific uptake of FA-2DG-D-Cy5 and 2DG-D-Cy5 was observed primarily in the liver and kidneys (**Figure 3B-C**). For more precise quantification, frozen tissue samples from the 1, 6, 24, and 72-hour groups were homogenized, and fluorescence intensity was measured to assess quantitative dendrimer uptake in lesions and major organs. Both FA-2DG-D-Cy5 and 2DG-D-Cy5 showed strong, persistent accumulation within endometriosis lesions beginning at 1-hour post-injection and sustained through 72 hours **(Figures 3D and S16)**. By 72 hours, lesion uptake of FA-2DG-D-Cy5 was significantly higher than that of 2DG-D-Cy5, suggesting its targeted accumulation in FR$\beta^+$ macrophages that are abundant in endometriotic lesions (**Figure 3D-E and Supplementary Figure S16**). Moreover, FA-2DG-D-Cy5 demonstrated minimal accumulation (<5% Injected Dose (% I.D.)) in other major organs, indicating rapid clearance from off-target tissues **(Figure 3E)**. Importantly, unlike many nanoparticle systems that exhibit up to ~80% hepatic accumulation, FA-2DG-D-Cy5 showed only ~4% liver accumulation, comparable to the previously characterized 2DG-D-Cy5 platform, demonstrating its favorable pharmacokinetic profile [27].

### *3.4. Confocal Imaging of Cellular Uptake of Intraperitoneally Administered FA-2DG-D-Cy5 and 2DG-D-Cy5 in a Mouse Model of Endometriosis*

We next examined the targeting ability, including selective cellular uptake, localization, and retention of FA-2DG-D-Cy5 or 2DG-D-Cy5 in ELL-induced mice 2 weeks after dendrimer administration (**Figure 4**). Confocal imaging showed that FA-2DGD-Cy5 (red) was selectively targeted and taken up by FR$\beta^+$ macrophages (green), not only in lesions but also in peritoneal exudate cells (**Figure 4A-B, white arrows**), where FR$\beta^+$ macrophages were elevated in ELL-induced mice. In contrast, cellular uptake of 2DG-D-Cy5 without FA ligand was limited in the

452 lesion and peritoneal cells (**Figure 4A-B**). Given the potential uptake of non-targeted 2DG-D-Cy5
453 by activated macrophages [28], we further quantified nonspecific FA-2DG-D-Cy5 internalization
454 in peritoneal exudate cells. The uptake was an average of 0.59%, indicating minimal nonspecific
455 internalization. No dendrimer retention was observed in the kidneys, liver, or spleen in ELL-
456 induced mice 2 weeks following dendrimer administration **(Figure 4C)**, indicating that FA-2DG-
457 D-Cy5 underwent complete clearance, and off-target accumulation in major organs was negligible.
458 These results suggest that FA-2DGD-Cy5 dendrimer is internalized only by ligand-receptor
459 endocytosis in FR$\beta^+$ macrophages in the lesions and peritoneal cells. As it remains stable within
460 cells for at least 2 weeks, it functions as an excellent nanocarrier for drug delivery.
461

462 ***3.5. Synthesis and Characterization of FA-2DG-D-Niclo Conjugate Using Click Chemistry***

463 We developed a niclosamide-labeled dendrimer platform, FA-2DG-D-Niclo, by
464 conjugating niclosamide to the FA-2DG-D, to enable targeted delivery of niclosamide to disease-
465 driving FR$\beta^+$ macrophages as a therapy for endometriosis. To achieve high conjugation efficiency
466 and precise drug loading, CuAAC was employed. A niclosamide bearing an azide linker (Niclo-
467 Azide) was first synthesized by functionalizing the phenolic -OH group of niclosamide (**Figure**
468 **5A**). Several linker architectures were explored to identify a construct that combined physiological
469 stability with controlled intracellular release. Initially, aliphatic and PEG-based carboxylic acids
470 were coupled to niclosamide through EDC/DMAP-mediated esterification, aiming to generate
471 ester linkages that are labile in the intracellular conditions and stable at physiological pH.
472 However, due to the proximity of the ester group to the aromatic ring, the resulting phenolic esters
473 exhibited instability and underwent rapid cleavage during subsequent CuAAC reactions [63]. To
474 circumvent this issue, a previous report on a disulfide-linker-based niclosamide prodrug was
475 followed with some modifications to design and synthesize niclosamide-azide (niclo-azide)
476 containing a disulfide linker [64]. It was reported that the disulfide linker remains stable under
477 extracellular conditions but undergoes selective cleavage in the intracellular environment, thereby
478 releasing free niclosamide [64].

479 The synthesis of niclo-azide was carried out through a multistep route (**Figure 5A**). The
480 Boc-protected disulfide derivative **(10)** was synthesized using a published procedure [64]. It was
481 then deprotected using 4 N HCl in dioxane to afford compound **11** as the amine hydrochloride salt,
482 which was directly converted to the corresponding carbamoyl chloride intermediate **12** using

483 triphosgene, following coupling with niclosamide **(13)** under mild basic conditions to afford the
484 desired Niclo-Azide **(14) (Figure 5A)**. Successful formation of the product was confirmed by
485 comparative integration in $^{1}$H NMR spectroscopy, which showed characteristic aromatic protons
486 from the niclosamide scaffold δ 8.4-7.3 ppm (6H) and the aliphatic protons from the disulfide
487 linker between δ 3.7-2.7 ppm (11H) **(Figures 5B and Supplementary Figure S19)**. The product
488 purity (~ 95.9%), was verified by HPLC, which showed a chromatogram with a retention time of
489 14.7 minutes **(Figures 6A and Supplementary Figure S21).** To enable subsequent CuAAC
490 coupling, 2DG-D **(4)** was partially modified with 5-hexynoic acid. Approximately 12 hydroxyl
491 groups per dendrimer were modified to yield 2DG-D-Hexyne' **(15) (Figure 5A)**. The formation of
492 the required product was confirmed by the appearance of characteristic methylene proton signals
493 from the hexynoic linker in the aliphatic region of the $^{1}$H NMR spectrum at δ 1.7 (24H), 2.4 (24H)
494 and at 2.2 ppm **(Figures 5B and Supplementary Figure S23)** which confirmed the presence of
495 12 hexyne arms. HPLC analysis of 2DG-D-Hexyne' **(15)** showed the chromatogram at 10.4
496 minutes with a purity exceeding 97% **(Figure 6A)**. Subsequently, a CuAAC reaction between FA-
497 Azide **(3)** and 2DG-D-Hexyne' **(15)** yielded FA-2DG-D' **(16)**. The $^{1}$H NMR spectrum of FA-2DG-
498 D' **(16)** showed characteristic aromatic resonances corresponding to folic acid, confirming
499 successful conjugation of 2 molecules per dendrimer **(Supplementary Figure S26).** The resulting
500 construct retained approximately ten free terminal alkyne groups per dendrimer. The HPLC
501 chromatogram exhibited a retention time shift from 10.4 minutes for 2DG-D-Hexyne' to 9.5
502 minutes for FA-2DG-D' **(16)**, with a purity of ~99% **(Figures 6A and Supplementary Figure**
503 **S28)**. Lastly, FA-2DG-D' **(16)** was conjugated with Niclo-Azide **(14)** through CuAAC to obtain
504 FA-2DG-D-Niclo **(17)**. Consistent with our previous studies [56, 58], we aimed to maintain the
505 drug loading between 10 and 15% to ensure aqueous solubility of the dendrimer conjugate. Drug
506 loading was calculated by $^{1}$H NMR spectroscopy through comparison of the dendrimer aromatic
507 protons at δ 7.2 ppm (16H) with the newly aromatic signals at δ 8.4 (10H), 8.3 (10H), and 8.2-7.8
508 ppm, along with distinct amide protons of niclosamide at δ 10.43 ppm (10H), confirmed the
509 conjugation of approximately ten niclosamide molecules per dendrimer, corresponding to ~12%
510 drug loading by weight **(Figures 5B and Supplementary Figure S29)**. HPLC analysis revealed a
511 shift in retention time from 9.5 minutes for FA-2DG-D' **(17)** to 11.2 minutes for FA-2DG-D-Niclo
512 **(17)**, with a final purity of more than 98% **(Supplementary Figure S31)**. DLS analysis indicated

513 a hydrodynamic diameter of 7.6 ± 0.6 nm and a zeta potential of -7.7 ± 0.6 mV **(Figure 6C and**
514 **Supplementary Figures S32 and S33)**.

515 The physicochemical properties of FA-2DG-D-Niclo **(23)** are presented in **Figure 7A.**
516 While niclosamide is practically insoluble in water (~5 µg/mL) [65], the dendrimer-drug conjugate
517 exhibited excellent aqueous solubility (~150 mg/mL). At a drug loading of 12%, this corresponds
518 to an effective niclosamide solubility of approximately 18 mg/mL in water, representing a ~3,600
519 fold increase in solubility compared to free niclosamide **(Figure 7A)**.

520 The shelf stability of FA-2DG-D-Niclo **(17)** (1 mg/mL) was assessed in PBS at 4 °C, room
521 temperature (25 °C), and 40 °C over a 30-day period. The formulation remained stable throughout
522 the study, retaining more than 96% purity by HPLC at all tested temperatures **(Supplementary**
523 **Figure S34)**. No shifts in retention time were observed over 30 days, confirming the chemical
524 stability of the formulation under these conditions.

525 ***3.6. Scalable and Reproducible Synthesis of FA-2DG-D-Niclo***

526 Ensuring synthetic reproducibility and scalability remains a central barrier in advancing
527 nanoparticle-based therapeutics toward clinical applications. To overcome these challenges, we
528 established a streamlined and scalable synthetic workflow for FA-2DG-D-Niclo **(17)** that enables
529 rigorous characterization of intermediates at each stage. To assess batch-to-batch consistency, three
530 independent 400 mg-scale batches were synthesized and evaluated by $^{1}$H NMR and HPLC. The
531 $^{1}$H NMR spectra of all three batches **(Figure 7B, left)** showed identical chemical profiles and
532 consistent drug and ligand loading. Similarly, HPLC analysis revealed overlapping chromatogram
533 peaks with retention times of ~11.2 minutes and purities exceeding 98%, confirming robust batch-
534 to-batch reproducibility **(Figure 7B, right)**.

535

536 ***3.7. In vitro drug release studies for FA-2DG-D-Niclo***

537 We further assessed the in vitro drug-release profile of the conjugate under conditions
538 mimicking both the extracellular environment (PBS + 0.1 mM GSH and 100% human plasma) and
539 the intracellular microenvironment (pH 5.5 citrate buffer + 10mM GSH) **(Figure 7C)**. Since
540 niclosamide is attached to the dendrimer through a disulfide linkage, it enables glutathione (GSH)
541 responsive cleavage [66]. Upon cleavage, the generated free thiol is known to undergo an
542 intramolecular nucleophilic attack on the tertiary carbamate, ultimately yielding free niclosamide

543 [64]. When conjugated to the targeted FA-2DG-D, this design facilitates controlled release within
544 the intracellular environments while limiting premature systemic exposure outside the lesion sites.
545 In PBS and 0.1mM GSH, the conjugate was found to be relatively stable. Less than 40% of the
546 drug was observed to be released in around 2 weeks, with <10% drug release detected for the first
547 5 days. Notably less than 5% of the drug was released within 8 hours. When incubated in human
548 plasma, less than 35% of the drug was released over 5 days, indicating stability in physiological
549 conditions **(Figure 7C).** Under intracellular conditions (pH 5.5 citrate buffer + 10mM GSH), the
550 conjugate showed a sustained release profile, with ~45% released in the first 24 hours, ~80% by
551 two days, and reaching ~95% over 12 days **(Figure 7C)**. The targeted and sustained intracellular
552 drug release profile is important to maintain the efficacy of the drug for a long time and to avoid
553 off-target effects.
554

555 ***3.8. FA-2DG-D-Niclo attenuates lesion progression and endometriosis-associated hyperalgesia.***

556 Lastly, we assessed the efficacy of FA-2DG-D-Niclo in endometriosis disease progression
557 and endometriosis-associated hyperalgesia. After the lesion induction, a single dose of FA-2DG-
558 D-Niclo dendrimer (25 or 50 mg/kg bw of niclosamide) or FA-2DG-D without niclosamide control
559 was administered i.p. in ELL-induced mice at Day 7, as shown in **Figure 8A**. Then, the efficacy
560 of dendrimers was examined 7 (Day 14) and 14 (Day 21) days after dendrimer administration. We
561 first confirmed the suppressing capability of FR$\beta^+$ macrophages in the lesions and peritoneal cavity
562 by FA-2DG-D-Niclo dendrimer (**Figure 8B-C**). Single dosing of FA-2DG-D-Niclo (50 mg/kg bw)
563 significantly reduced FR$\beta^+$ macrophages in the lesions at Day 21, although the reduction of FR$\beta^+$
564 macrophages was not observed at Day 14 (**Figure 8B**). Peritoneal FR$\beta^+$ macrophage population
565 was reduced by both doses (25 and 50 mg/kg bw) of FA-2DG-D-Niclo (**Figure 8C**). The results
566 indicate that 7 days after dendrimer administration may not be sufficient to reduce FR$\beta^+$
567 macrophages in both lesions and the peritoneum. Indeed, lesion number and volume were also
568 significantly reduced at Day 21 by FA-2DG-D-Niclo at both doses, but there were no significant
569 differences in lesion number or volume at Day 14 (**Figure 9A**). However, we realized that three
570 mice treated with both doses and examined at Day 14 did not have lesions. Furthermore, four and
571 five mice, at doses of 25 and 50 mg/kg bw of niclosamide, respectively, did not have lesions by
572 Day 21, either. Thus, a single dose of FA-2DG-D-Niclo administration completely inhibited lesion
573 growth and progression in 37.5-62.5% of mice, whereas all control mice developed lesions on

574 Days 14 and 21. While reduced FRβ$^+$ macrophages in the remaining lesions were observed only
575 at Day 21, a few mice at Day 14 lacked lesions for examination, suggesting that FA-2DG-D-Niclo
576 was likely effective for lesion growth 7 days after administration. In support of this implication,
577 abdominal and hindpaw hypersensitivities were already improved at Day 14 (**Figure 9B**). The
578 abdominal and hindpaw sensitivity 7 days after lesion induction was high compared to before
579 lesion induction (Day -1). At Day 14, FA-2DG-D-Niclo at a dose of 50 mg/kg bw of niclosamide
580 significantly reduced the abdominal sensitivity, which is considered indicative of peripheral
581 visceral pain. Both doses of FA-2DG-D-Niclo improved hindpaw sensitivity, which is likely be
582 affected by peripheral and central sensitization. By Day 21, FA-2DG-D-Niclo at both doses further
583 improved abdominal and hindpaw sensitivities. The results clearly showed that a single dose of
584 FA-2DG-D-Niclo inhibited disease progression and endometriosis-associated hyperalgesia.
585 Notably, a single dose of FA-2DG-D-Niclo remained effective for 2 weeks after administration.
586 The current FDA-approved niclosamide treatment requires a high dose (2g/day) due to its low
587 water solubility and is limited to oral administration for 7 days. Niclosamide treatment for patients
588 who have endometriosis would need to be longer due to the chronic nature of the disease. Long-
589 term systemic treatment with niclosamide could cause off-target actions. Therefore, the 2DG-D-
590 based delivery of niclosamide and targeting of disease-specific FRβ$^+$ macrophages is highly
591 translational, as FA-2DG-D can deliver niclosamide intracellularly into FRβ$^+$ macrophages,
592 thereby enhancing efficacy, reducing side effects, and treating chronic diseases such as
593 endometriosis.
594
595 **4. Conclusions**
596 With integrated single-cell transcriptomic analysis, we further identified a significant
597 recruitment of pro-disease FRβ$^+$ macrophages within human endometriotic lesions and the pelvic
598 cavity, mirroring our observations in the mouse model. Importantly, overexpression of FRβ on
599 these macrophages provides a ligand-guided entry point, enabling receptor-specific targeting for
600 both imaging and therapeutic interventions. Leveraging this receptor overexpression, we
601 engineered a folic acid-conjugated dendrimer (FA-2DG-D) to exploit FRβ-mediated uptake for
602 targeted imaging and drug delivery in endometriotic lesions. FA-2DG-D offers several critical
603 advantages for translational development. The dendrimer architecture enables precise,
604 reproducible conjugation of targeting ligands and therapeutic payloads via click chemistry,

resulting in well-defined nanostructures, excellent aqueous solubility, and robust batch-to-batch consistency. Conjugation of niclosamide to generate FA-2DG-D-Niclo markedly enhanced the solubility of this poorly water-soluble drug, enabled controlled, intracellularly triggered release via a disulfide linker, and minimized premature systemic exposure. Importantly, the formulation demonstrated high stability under physiological and storage conditions. In a mouse model of endometriosis, the Cy5-labelled platform demonstrated lesion and peritoneal cell-specific accumulation and intracellular internalization along with a favorable biodistribution with minimal off-target organ accumulation. FA-2DG-D-Niclo enabled targeted delivery to disease-driving macrophages. Administration of FA-2DG-D-Niclo led to significant reductions in lesion number and volume, and improved hyperalgesia, highlighting both therapeutic efficacy and immunomodulatory activity. This work demonstrates the potential of FA-2DG-D platform to target FR$\beta^+$ macrophages for the treatment of endometriosis. By addressing key limitations of current hormonal and systemic treatments, this approach establishes a non-hormonal, FR$\beta^+$ macrophage-focused strategy for the treatment of endometriosis.

**Supporting Information**

The chemistry experimental details and supplementary figures related to characterization, stability studies, and bioditribution are provided in supporting information.

**Data Availability Statement**

The raw data of scRNA sequencing have been deposited to NCBI/SRA (PRJNA1418167). Additional data or materials related to the findings of this study are available from the corresponding author upon reasonable request.

**Funding Information**

This work was supported by NIH grant R01HD104619 (to Kanako Hayashi) and a Washington Research Foundation Technology Commercialization Phase 1 award (to Kanako Hayashi and Anjali Sharma).

**Declaration of Interest Statement:**

The authors A.S, K.H, R.S, A.D, M.S, M.E.H, and A.I.D have pending patents and invention disclosures on 2DG and/or FA-2DG dendrimers and their conjugates.

**Authorship Contribution Statement**

A.S. and K.H. designed the research; A.D., A.S., and R.S. designed and synthesized the dendrimers; M.S., M.H., and T.P. performed the animal experiments and/or analyzed the data; A.D., K.J.G., and A.I.D. performed quantitative biodistribution analysis; N.S.M., V.K.S., and P.S.C. collected/or prepared the human samples; M.S. performed single-cell RNA sequencing and analysis; A.D., M.S., R.S., A.S., and K.H. wrote the paper; all authors read, reviewed, edited, and approved the manuscript.

## References


1. Zondervan, K. T.; Becker, C. M.; Missmer, S. A. **Endometriosis**. *The New England journal of medicine* 2020, **382**, (13), 1244-1256.
2. Burney, R. O.; Giudice, L. C. **Pathogenesis and pathophysiology of endometriosis**. *Fertility and sterility* 2012, **98**, (3), 511-9.
3. As-Sanie, S.; Mackenzie, S. C.; Morrison, L.; Schrepf, A.; Zondervan, K. T.; Horne, A. W.; Missmer, S. A. **Endometriosis: A Review**. *JAMA* 2025, **334**, (1), 64-78.
4. Giudice, L. C.; Kao, L. C. **Endometriosis**. *Lancet (London, England)* 2004, **364**, (9447), 1789-99.
5. Ellis, K.; Munro, D.; Clarke, J. **Endometriosis Is Undervalued: A Call to Action**. *Frontiers in global women's health* 2022, **3**, 902371.
6. Marla, S.; Mortlock, S.; Heinosalo, T.; Poutanen, M.; Montgomery, G. W.; McKinnon, B. D. **Gene expression profiles separate endometriosis lesion subtypes and indicate a sensitivity of endometrioma to estrogen suppressive treatments through elevated ESR2 expression**. *BMC Medicine* 2023, **21**, (1), 460.
7. Edi, R.; Cheng, T. **Endometriosis: Evaluation and Treatment**. *American family physician* 2022, **106**, (4), 397-404.
8. Alonso, A.; Gunther, K.; Maheux-Lacroix, S.; Abbott, J. **Medical management of endometriosis**. *Current opinion in obstetrics & gynecology* 2024, **36**, (5), 353-361.
9. Guo, S.-W. **Recurrence of endometriosis and its control**. *Human Reproduction Update* 2009, **15**, (4), 441-461.
10. Singh, S. S.; Gude, K.; Perdeaux, E.; Gattrell, W. T.; Becker, C. M. **Surgical Outcomes in Patients With Endometriosis: A Systematic Review**. *Journal of obstetrics and gynaecology Canada : JOGC = Journal d'obstetrique et gynecologie du Canada : JOGC* 2020, **42**, (7), 881-888.e11.
11. Sekulovski, N.; Whorton, A. E.; Shi, M.; MacLean, J. A., II; Hayashi, K. **Endometriotic inflammatory microenvironment induced by macrophages can be targeted by niclosamide†**. *Biology of reproduction* 2019, **100**, (2), 398-408.
12. Sekulovski, N.; Whorton, A. E.; Tanaka, T.; Hirota, Y.; Shi, M.; MacLean, J. A.; de Mola, J. R. L.; Groesch, K.; Diaz-Sylvester, P.; Wilson, T.; Hayashi, K. **Niclosamide suppresses macrophage-induced inflammation in endometriosis†**. *Biology of reproduction* 2020, **102**, (5), 1011-1019.
13. Shi, M.; Sekulovski, N.; Whorton, A. E.; MacLean, J. A., 2nd; Greaves, E.; Hayashi, K. **Efficacy of niclosamide on the intra-abdominal inflammatory environment in endometriosis**. *FASEB journal : official publication of the Federation of American Societies for Experimental Biology* 2021, **35**, (5), e21584.
14. Zhao, L.; Shi, M.; Winuthayanon, S.; MacLean, J. A., 2nd; Hayashi, K. **Niclosamide targets the dynamic progression of macrophages for the resolution of endometriosis in a mouse model**. *Communications biology* 2022, **5**, (1), 1225.
15. Tan, Y.; Flynn, W. F.; Sivajothi, S.; Luo, D.; Bozal, S. B.; Davé, M.; Luciano, A. A.; Robson, P.; Luciano, D. E.; Courtois, E. T. **Single-cell analysis of endometriosis reveals a coordinated transcriptional programme driving immunotolerance and angiogenesis across eutopic and ectopic tissues**. *Nature cell biology* 2022, **24**, (8), 1306-1318.
16. Prather, G. R.; MacLean, J. A., 2nd; Shi, M.; Boadu, D. K.; Paquet, M.; Hayashi, K. **Niclosamide As a Potential Nonsteroidal Therapy for Endometriosis That Preserves**

692 **Reproductive Function in an Experimental Mouse Model**. *Biology of reproduction* 2016, **95**,
693 (4), 76.
694 17. Chen, W.; Mook, R. A., Jr.; Premont, R. T.; Wang, J. **Niclosamide: Beyond an**
695 **antihelminthic drug**. *Cellular signalling* 2018, **41**, 89-96.
696 18. Jug, M.; Laffleur, F.; Millotti, G. **Revisiting Niclosamide Formulation Approaches - a**
697 **Pathway Toward Drug Repositioning**. *Drug design, development and therapy* 2024, **18**, 4153-
698 4182.
699 19. Rani, A.; Bisen, S.; Sharma, R.; Dar, A. I.; Sharma, A.; Dhull, A.; Palmer, N.; Goody, K.
700 J.; Singh, N. K.; Sharma, A. **Systemic targeting of aberrant neovascular tufts using trehalose-**
701 **dendrimer nanocarriers for the treatment of proliferative retinopathies**. *Theranostics* 2026,
702 **16**, (3), 1504-1527.
703 20. Pulukuri, A. J.; Dhull, A.; Dar, A. I.; Rani, A.; Sharma, R.; Berkman, C. E.; Sharma, A.
704 **Dendrimer-Mediated Delivery Enhances Therapeutic Efficacy in Triple-Negative Breast**
705 **Cancer**. *Biomacromolecules* 2025, **26**, (9), 5979-6000.
706 21. Sharma, R.; Porterfield, J. E.; An, H.-T.; Jimenez, A. S.; Lee, S.; Kannan, S.; Sharma, A.;
707 Kannan, R. M. **Rationally Designed Galactose Dendrimer for Hepatocyte-Specific Targeting**
708 **and Intracellular Drug Delivery for the Treatment of Liver Disorders**. *Biomacromolecules*
709 2021, **22**, (8), 3574-3589.
710 22. Monge, P.; Søgaard, A. B.; Andersen, D. G.; Chandrawati, R.; Zelikin, A. N. **Synthetic**
711 **chemical ligands and cognate antibodies for biorthogonal drug targeting and cell**
712 **engineering**. *Advanced Drug Delivery Reviews* 2021, **170**, 281-293.
713 23. Nam, H. Y.; Nam, K.; Hahn, H. J.; Kim, B. H.; Lim, H. J.; Kim, H. J.; Choi, J. S.; Park, J.-
714 S. **Biodegradable PAMAM ester for enhanced transfection efficiency with low cytotoxicity**.
715 *Biomaterials* 2009, **30**, (4), 665-673.
716 24. Huang, W.-C.; Lu, I. L.; Chiang, W.-H.; Lin, Y.-W.; Tsai, Y.-C.; Chen, H.-H.; Chang, C.-
717 W.; Chiang, C.-S.; Chiu, H.-C. **Tumortropic adipose-derived stem cells carrying smart**
718 **nanotherapeutics for targeted delivery and dual-modality therapy of orthotopic**
719 **glioblastoma**. *Journal of Controlled Release* 2017, **254**, 119-130.
720 25. Dhull, A.; Yu, C.; Wilmoth, A. H.; Chen, M.; Sharma, A.; Yiu, S. **Dendrimers in Corneal**
721 **Drug Delivery: Recent Developments and Translational Opportunities**. *Pharmaceutics* 2023,
722 **15**, (6).
723 26. Dhull, A.; Wei, J.; Pulukuri, A. J.; Rani, A.; Sharma, R.; Mesbahi, N.; Yoon, H.; Savoy, E.
724 A.; Xaivong Vi, S.; Goody, K. J.; Berkman, C. E.; Wu, B. J.; Sharma, A. **PSMA-targeted**
725 **dendrimer as an efficient anticancer drug delivery vehicle for prostate cancer**. *Nanoscale*
726 2024, **16**, (11), 5634-5652.
727 27. Dhull, A.; Zhang, Z.; Sharma, R.; Dar, A. I.; Rani, A.; Wei, J.; Gopalakrishnan, S.;
728 Ghannam, A.; Hahn, V.; Pulukuri, A. J.; Tasevski, S.; Moughni, S.; Wu, B. J.; Sharma, A.
729 **Discovery of 2-deoxy glucose surfaced mixed layer dendrimer: a smart neuron targeted**
730 **systemic drug delivery system for brain diseases**. *Theranostics* 2024, **14**, (8), 3221-3245.
731 28. Dhull, A.; Park, K. W.; Dar, A. I.; Wang, A.; Rani, A.; Sharma, R.; Valdez, T. A.; Sharma,
732 A. **Mixed-Layered Glycodendrimer Probe for Imaging Inflammation at Surgical Site**
733 **Infections**. *ACS Sensors* 2025, **10**, (3), 2234-2243.
734 29. Puligujja, P.; McMillan, J.; Kendrick, L.; Li, T.; Balkundi, S.; Smith, N.; Veerubhotla, R.
735 S.; Edagwa, B. J.; Kabanov, A. V.; Bronich, T.; Gendelman, H. E.; Liu, X. M. **Macrophage folate**
736 **receptor-targeted antiretroviral therapy facilitates drug entry, retention, antiretroviral**

**activities and biodistribution for reduction of human immunodeficiency virus infections**. *Nanomedicine : nanotechnology, biology, and medicine* 2013, **9**, (8), 1263-73.
30. Chandrupatla, D.; Molthoff, C. F. M.; Lammertsma, A. A.; van der Laken, C. J.; Jansen, G. **The folate receptor β as a macrophage-mediated imaging and therapeutic target in rheumatoid arthritis**. *Drug delivery and translational research* 2019, **9**, (1), 366-378.
31. Zheng, G. X.; Terry, J. M.; Belgrader, P.; Ryvkin, P.; Bent, Z. W.; Wilson, R.; Ziraldo, S. B.; Wheeler, T. D.; McDermott, G. P.; Zhu, J.; Gregory, M. T.; Shuga, J.; Montesclaros, L.; Underwood, J. G.; Masquelier, D. A.; Nishimura, S. Y.; Schnall-Levin, M.; Wyatt, P. W.; Hindson, C. M.; Bharadwaj, R.; Wong, A.; Ness, K. D.; Beppu, L. W.; Deeg, H. J.; McFarland, C.; Loeb, K. R.; Valente, W. J.; Ericson, N. G.; Stevens, E. A.; Radich, J. P.; Mikkelsen, T. S.; Hindson, B. J.; Bielas, J. H. **Massively parallel digital transcriptional profiling of single cells**. *Nature communications* 2017, **8**, 14049.
32. Wang, W.; Vilella, F.; Alama, P.; Moreno, I.; Mignardi, M.; Isakova, A.; Pan, W.; Simon, C.; Quake, S. R. **Single-cell transcriptomic atlas of the human endometrium during the menstrual cycle**. *Nature medicine* 2020, **26**, (10), 1644-1653.
33. Lai, Z. Z.; Wang, Y.; Zhou, W. J.; Liang, Z.; Shi, J. W.; Yang, H. L.; Xie, F.; Chen, W. D.; Zhu, R.; Zhang, C.; Mei, J.; Zhao, J. Y.; Ye, J. F.; Zhang, T.; Li, M. Q. **Single-cell transcriptome profiling of the human endometrium of patients with recurrent implantation failure**. *Theranostics* 2022, **12**, (15), 6527-6547.
34. Garcia-Alonso, L.; Handfield, L. F.; Roberts, K.; Nikolakopoulou, K.; Fernando, R. C.; Gardner, L.; Woodhams, B.; Arutyunyan, A.; Polanski, K.; Hoo, R.; Sancho-Serra, C.; Li, T.; Kwakwa, K.; Tuck, E.; Lorenzi, V.; Massalha, H.; Prete, M.; Kleshchevnikov, V.; Tarkowska, A.; Porter, T.; Mazzeo, C. I.; van Dongen, S.; Dabrowska, M.; Vaskivskyi, V.; Mahbubani, K. T.; Park, J. E.; Jimenez-Linan, M.; Campos, L.; Kiselev, V. Y.; Lindskog, C.; Ayuk, P.; Prigmore, E.; Stratton, M. R.; Saeb-Parsy, K.; Moffett, A.; Moore, L.; Bayraktar, O. A.; Teichmann, S. A.; Turco, M. Y.; Vento-Tormo, R. **Mapping the temporal and spatial dynamics of the human endometrium in vivo and in vitro**. *Nature genetics* 2021, **53**, (12), 1698-1711.
35. Fonseca, M. A. S.; Haro, M.; Wright, K. N.; Lin, X.; Abbasi, F.; Sun, J.; Hernandez, L.; Orr, N. L.; Hong, J.; Choi-Kuaea, Y.; Maluf, H. M.; Balzer, B. L.; Fishburn, A.; Hickey, R.; Cass, I.; Goodridge, H. S.; Truong, M.; Wang, Y.; Pisarska, M. D.; Dinh, H. Q.; El-Naggar, A.; Huntsman, D. G.; Anglesio, M. S.; Goodman, M. T.; Medeiros, F.; Siedhoff, M.; Lawrenson, K. **Single-cell transcriptomic analysis of endometriosis**. *Nature genetics* 2023, **55**, (2), 255-267.
36. Huang, X.; Wu, L.; Pei, T.; Liu, D.; Liu, C.; Luo, B.; Xiao, L.; Li, Y.; Wang, R.; Ouyang, Y.; Zhu, H.; Huang, W. **Single-cell transcriptome analysis reveals endometrial immune microenvironment in minimal/mild endometriosis**. *Clinical and experimental immunology* 2023, **212**, (3), 285-295.
37. Marečková, M.; Garcia-Alonso, L.; Moullet, M.; Lorenzi, V.; Petryszak, R.; Sancho-Serra, C.; Oszlanczi, A.; Icoresi Mazzeo, C.; Wong, F. C. K.; Kelava, I.; Hoffman, S.; Krassowski, M.; Garbutt, K.; Gaitskell, K.; Yancheva, S.; Woon, E. V.; Male, V.; Granne, I.; Hellner, K.; Mahbubani, K. T.; Saeb-Parsy, K.; Lotfollahi, M.; Prigmore, E.; Southcombe, J.; Dragovic, R. A.; Becker, C. M.; Zondervan, K. T.; Vento-Tormo, R. **An integrated single-cell reference atlas of the human endometrium**. *Nature genetics* 2024, **56**, (9), 1925-1937.
38. Shin, S.; Chung, Y. J.; Moon, S. W.; Choi, E. J.; Kim, M. R.; Chung, Y. J.; Lee, S. H. **Single-cell profiling identifies distinct hormonal, immunologic, and inflammatory signatures of endometriosis-constituting cells**. *The Journal of pathology* 2023, **261**, (3), 323-334.

39. Han, J.; Gallerand, A.; Erlich, E. C.; Helmink, B. A.; Mair, I.; Li, X.; Eckhouse, S. R.; Dimou, F. M.; Shakhsheer, B. A.; Phelps, H. M.; Chan, M. M.; Mintz, R. L.; Lee, D. D.; Schilling, J. D.; Finlay, C. M.; Allen, J. E.; Jakubzick, C. V.; Else, K. J.; Onufer, E. J.; Zhang, N.; Randolph, G. J. **Human serous cavity macrophages and dendritic cells possess counterparts in the mouse with a distinct distribution between species**. *Nature immunology* 2024, **25**, (1), 155-165.
40. Zou, G.; Wang, J.; Xu, X.; Xu, P.; Zhu, L.; Yu, Q.; Peng, Y.; Guo, X.; Li, T.; Zhang, X. **Cell subtypes and immune dysfunction in peritoneal fluid of endometriosis revealed by single-cell RNA-sequencing**. *Cell & bioscience* 2021, **11**, (1), 98.
41. Wolf, F. A.; Angerer, P.; Theis, F. J. **SCANPY: large-scale single-cell gene expression data analysis**. *Genome biology* 2018, **19**, (1), 15.
42. Wolock, S. L.; Lopez, R.; Klein, A. M. **Scrublet: Computational Identification of Cell Doublets in Single-Cell Transcriptomic Data**. *Cell systems* 2019, **8**, (4), 281-291.e9.
43. Giotti, B.; Chen, S. H.; Barnett, M. W.; Regan, T.; Ly, T.; Wiemann, S.; Hume, D. A.; Freeman, T. C. **Assembly of a parts list of the human mitotic cell cycle machinery**. *Journal of molecular cell biology* 2019, **11**, (8), 703-718.
44. Korsunsky, I.; Millard, N.; Fan, J.; Slowikowski, K.; Zhang, F.; Wei, K.; Baglaenko, Y.; Brenner, M.; Loh, P. R.; Raychaudhuri, S. **Fast, sensitive and accurate integration of single-cell data with Harmony**. *Nature methods* 2019, **16**, (12), 1289-1296.
45. Traag, V. A.; Waltman, L.; van Eck, N. J. **From Louvain to Leiden: guaranteeing well-connected communities**. *Scientific reports* 2019, **9**, (1), 5233.
46. Soneson, C.; Robinson, M. D. **Bias, robustness and scalability in single-cell differential expression analysis**. *Nature methods* 2018, **15**, (4), 255-261.
47. Wu, C.; Boey, D.; Bril, O.; Grootens, J.; Vijayabaskar, M. S.; Sorini, C.; Ekoff, M.; Wilson, N. K.; Ungerstedt, J. S.; Nilsson, G.; Dahlin, J. S. **Single-cell transcriptomics reveals the identity and regulators of human mast cell progenitors**. *Blood advances* 2022, **6**, (15), 4439-4449.
48. Panjwani, M. K.; Grassmann, S.; Sottile, R.; Le Luduec, J. B.; Kontopoulos, T.; van der Ploeg, K.; Sun, J. C.; Hsu, K. C. **Single-cell profiling aligns CD56(bright) and cytomegalovirus-induced adaptive natural killer cells to a naïve-memory relationship**. *Frontiers in immunology* 2024, **15**, 1499492.
49. Yu, G.; Wang, L. G.; Han, Y.; He, Q. Y. **clusterProfiler: an R package for comparing biological themes among gene clusters**. *Omics : a journal of integrative biology* 2012, **16**, (5), 284-7.
50. Nothnick, W. B.; Colvin, A.; Cheng, K. F.; Al-Abed, Y. **Inhibition of macrophage migration inhibitory factor reduces endometriotic implant size in mice with experimentally induced disease**. *Journal of endometriosis* 2011, **3**, (3), 135-142.
51. Herup-Wheeler, T.; Shi, M.; Harvey, M. E.; Talwar, C.; Kommagani, R.; MacLean, J. A., 2nd; Hayashi, K. **High-fat diets promote peritoneal inflammation and augment endometriosis-associated abdominal hyperalgesia**. *Frontiers in endocrinology* 2024, **15**, 1336496.
52. Shi, M.; MacLean, J. A., 2nd; Hayashi, K. **The involvement of peritoneal GATA6(+) macrophages in the pathogenesis of endometriosis**. *Frontiers in immunology* 2024, **15**, 1396000.
53. Davies, L. C.; Rice, C. M.; Palmieri, E. M.; Taylor, P. R.; Kuhns, D. B.; McVicar, D. W. **Peritoneal tissue-resident macrophages are metabolically poised to engage microbes using tissue-niche fuels**. *Nature communications* 2017, **8**, (1), 2074.

54. Vega-Pérez, A.; Villarrubia, L. H.; Godio, C.; Gutiérrez-González, A.; Feo-Lucas, L.; Ferriz, M.; Martínez-Puente, N.; Alcaín, J.; Mora, A.; Sabio, G.; López-Bravo, M.; Ardavín, C. **Resident macrophage-dependent immune cell scaffolds drive anti-bacterial defense in the peritoneal cavity**. *Immunity* 2021, **54**, (11), 2578-2594.e5.
55. Jiang, D.; Xiao, R.; Bai, J.; Wang, X.; Fang, Y.; Liu, J.; Wang, X.; Cui, M.; You, L.; Zhao, Y. **FOLR2(+) macrophages in cancer: allies or enemies**. *Cell communication and signaling : CCS* 2025, **23**, (1), 261.
56. Rani, A.; Pulukuri, A. J.; Wei, J.; Dhull, A.; Dar, A. I.; Sharma, R.; Mesbahi, N.; Savoy, E. A.; Yoon, H.; Wu, B. J.; Berkman, C. E.; Sharma, A. **PSMA-Targeted 2-Deoxyglucose-Based Dendrimer Nanomedicine for the Treatment of Prostate Cancer**. *Biomacromolecules* 2024, **25**, (9), 6164-6180.
57. Dar, A. I.; Jain, V.; Rani, A.; Pulukuri, A. J.; Gonzalez, J. C.; Dhull, A.; Sharma, R.; Sharma, A. **Silibinin-Conjugated Galactose Dendrimers for Targeted Treatment of Hepatocellular Carcinoma**. *ACS Applied Materials & Interfaces* 2025, **17**, (14), 20980-21000.
58. Dar, A. I.; Zhang, Z.; Gopalakrishnan, S.; Sharma, R.; Pulukuri, A. J.; Rani, A.; Dhull, A.; Gonzalez, J. C.; Atoui, T.; Mashal, Y.; Naseer, Z.; Calmi, J.; Sharma, A. **Neuron-targeted 2-deoxyglucose-dendrimer-rosiglitazone nanotherapy mitigates neuroinflammation and cognitive deficits in pediatric traumatic brain injury**. *Bioengineering & Translational Medicine* **n/a**, (n/a), e70053.
59. Chen, C.; Ke, J.; Zhou, X. E.; Yi, W.; Brunzelle, J. S.; Li, J.; Yong, E. L.; Xu, H. E.; Melcher, K. **Structural basis for molecular recognition of folic acid by folate receptors**. *Nature* 2013, **500**, (7463), 486-9.
60. van Dongen, M. A.; Silpe, J. E.; Dougherty, C. A.; Kanduluru, A. K.; Choi, S. K.; Orr, B. G.; Low, P. S.; Banaszak Holl, M. M. **Avidity mechanism of dendrimer-folic acid conjugates**. *Molecular pharmaceutics* 2014, **11**, (5), 1696-706.
61. Hong, S.; Leroueil, P. R.; Majoros, I. J.; Orr, B. G.; Baker, J. R., Jr.; Banaszak Holl, M. M. **The binding avidity of a nanoparticle-based multivalent targeted drug delivery platform**. *Chemistry & biology* 2007, **14**, (1), 107-15.
62. Thomas, T. P.; Huang, B.; Choi, S. K.; Silpe, J. E.; Kotlyar, A.; Desai, A. M.; Zong, H.; Gam, J.; Joice, M.; Baker, J. R., Jr. **Polyvalent dendrimer-methotrexate as a folate receptor-targeted cancer therapeutic**. *Molecular pharmaceutics* 2012, **9**, (9), 2669-2676.
63. de Souza, H. M. R.; Guedes, J. S.; Freitas, R.; Gelves, L. G. V.; Fokoue, H. H.; Sant'Anna, C. M. R.; Barreiro, E. J.; Lima, L. M. **Comparative chemical and biological hydrolytic stability of homologous esters and isosteres**. *Journal of enzyme inhibition and medicinal chemistry* 2022, **37**, (1), 718-727.
64. Kim, J. H.; Park, S.; Jung, E.; Shin, J.; Kim, Y. J.; Kim, J. Y.; Sessler, J. L.; Seo, J. H.; Kim, J. S. **A dual-action niclosamide-based prodrug that targets cancer stem cells and inhibits TNBC metastasis**. *Proceedings of the National Academy of Sciences of the United States of America* 2023, **120**, (21), e2304081120.
65. Li, J.; Chang, Y.; Zou, Z. Z. **Enhancing the in vivo bioavailability and absorption of Niclosamide with amorphous solid dispersion via solvent method**. *RPS Pharmacy and Pharmacology Reports* 2024, **3**, (4).
66. Navath, R. S.; Kurtoglu, Y. E.; Wang, B.; Kannan, S.; Romero, R.; Kannan, R. M. **Dendrimer-drug conjugates for tailored intracellular drug release based on glutathione levels**. *Bioconjugate chemistry* 2008, **19**, (12), 2446-55.

874 **Figure and Legends**

875 ***Figure 1. scRNA-seq analysis of FOLR2$^+$ macrophages in endometrium and pelvic exudate cells***
876 ***in endometriosis.*** *(**A, B**) Lists of human scRNA-seq datasets analyzed and sample size per dataset*
877 *in the groups of (**A**) eutopic endometrium with (EuE) and without (Cont) endometriosis, ectopic*
878 *endometrium (lesion, EcE), and (**B**) pelvic exudate cells from subjects with (Endo) and without*
879 *(Cont) endometriosis. (**C, D**) UMAP plots showing major cell types identified in the endometrium*
880 *(EM) and pelvic cells (P). (**E, F**) Violin plot representing marker gene expression for each major*
881 *cell type identified in endometrial and pelvic cell datasets. (**G, H**) UMAP projections showing*
882 *expression patterns of FOLR2 in endometrial and pelvic cells. (**I, J**) Bar plots showing enriched*
883 *gene ontology (GO) biological processes in FOLR2$^+$ macrophages from endometrium and pelvic*
884 *cells. (**K, L**) Proportions of endometrial and pelvic FOLR2-expressing cells to total cells within*
885 *each tissue type. Differences among groups were analyzed with one-way ANOVA followed by the*
886 *Tukey multiple comparisons test. **P<0.01, ***P<0.001. (**M, N**) Dot plot showing representative*
887 *significantly differentially expressed genes (DEGs) involved in proinflammatory, angiogenesis,*
888 *and adhesion processes among groups of endometrium and pelvic cells (adjusted p-value <0.05).*

889

890 ***Figure 2. Preparation and structural elucidation of FA-2DG-D-Cy5 conjugate.*** *(**A**) Schematic*
891 *representation for the synthesis of FA-2DG-D-Cy5 using CuAAC reaction. Reagents and*
892 *conditions: (i) DMSO, DCC, NHS, DIPEA, RT, 12 hours, 70% (ii) DMF, EDC.HCl, DMAP, RT, 12*
893 *hours, 80% (iii) $CuSO_4.5H_2O$, Sodium ascorbate, DMF, DI Water, 60 $^oC$, 10 hours, 84% (iv)*
894 *$CuSO_4.5H_2O$, Sodium ascorbate, DMF, DI Water, 40 $^oC$, 6 hours, 88% (**B**) $^1H$ NMR spectra*
895 *showing characteristic proton signals of 2DG-D, 2DG-D-Hexyne, Folic Acid, FA-Azide, FA-2DG-*
896 *D and FA-2DG-D-Cy5 at each step of the synthesis.*

897

898 ***Figure 3. In vivo and ex vivo fluorescence imaging and whole-body biodistribution of FA-2DG-***
899 ***D-Cy5****. (**A**) Whole-body in vivo fluorescence images of mice following intravenous (tail vein)*
900 *administration of FA-2DG-D-Cy5 in sham controls (left) and ELL-induced mice (right), or 2DG-*
901 *D-Cy5 administered to ELL-induced mice (center) at 1, 6, 24, and 72 hours (n =*
902 *3/group/timepoint). (**B**) Ex vivo fluorescence images of major organs collected at 72 hours post-*
903 *injection. Organs are arranged from top to bottom as: brain, heart, spleen, lungs, liver, kidneys,*
904 *and lesion. (**C**) Quantitative analysis of in vivo fluorescence signals in major organs at 72 hours*
905 *(n = 3). (**D**) Heat map showing the mean percentage of injected dose (I.D.) in lesions and major*
906 *organs at 1, 6, 24, and 72 hours after FA-2DG-D-Cy5 administration in sham controls and ELL-*
907 *induced mice, or ELL-induced mice treated with 2DG-D-Cy5 (n=3/group). Heatmap was*
908 *generated with the ComplexHeatmap package of R. (**E**) Quantitative biodistribution of FA-2DG-*
909 *D-Cy5 and 2DG-D-Cy5 in lesions and major organs at 72 hours in sham and ELL-induced mice*
910 *(n = 3). Data for (D) and (E) were obtained by fluorescence spectroscopy of homogenized tissues*
911 *and are shown as the percentage of the injected dose per organ. Differences in each tissue among*
912 *groups for data in (C) and (E) were analyzed by one-way ANOVA followed by the Tukey multiple-*
913 *comparison test. $p < 0.05$ (*), $p < 0.01$ (**). ELL, endometriosis-like lesion.*

914

915 ***Figure 4. Cellular uptake of FA-2DG-D-Cy5 and 2DG-D-Cy5 at 2 weeks following***
916 ***intraperitoneal administration.*** *Representative images showing selective uptake of FA-2DG-D-*
917 *Cy5 or 2DG-D-Cy5 (**A**) in peritoneal cells, (**B**) in endometriosis-like lesions (ELL), and (**C**) kidney,*
918 *liver, and spleen from ELL-induced mice (n=3). Peritoneal cells were co-stained with FRβ (green)*
919 *and DAPI (blue). The Cy5 signal (red) was directly acquired using a confocal microscope. White*
920 *arrows denote Cy5-positive signal in $FR\beta^+$ cells.*

921

922 ***Figure 5. Preparation and structural elucidation of FA-2DG-D-Niclo conjugate.*** *(**A**) Schematic*
923 *representation for the synthesis of **(i)** Niclo-Azide and **(ii)** FA-2DG-D-Niclo using CuAAC reaction.*
924 *Reagents and conditions: (i) DCM, HCl, Dioxane, RT, 3 hours (ii) DCM, TEA, Triphosgene, -25*
925 *$^oC$, 1 hour (iii) DCM, TEA, DMAP, RT, 16 hours, 49% (iv) DMF, EDC.HCl, DMAP, RT, 12 hours,*
926 *82% (v) $CuSO_4.5H_2O$, Sodium ascorbate, DMF, DI Water, 60 $^oC$, 10 hours, 85% (vi) $CuSO_4.5H_2O$,*
927 *Sodium ascorbate, DMF, DI Water, 40 $^oC$, 10 hours, 75% (**B**) $^1H$ NMR spectra showing*

928 *characteristic proton signals of FA-2DG-D', Compound 10, Niclosamide, Niclo-Azide and FA-*
929 *2DG-D-Niclo at each step of the synthesis.*

930

931 ***Figure 6*. *Characterization of FA-2DG-D-Niclo conjugate and intermediates:*** *(**A**) HPLC*
932 *chromatograms of intermediates at various synthesis steps and percentage purity of FA-2DG-D-*
933 *Niclo. (**B**) (i) Hydrodynamic diameter, and (ii) Zeta Potential of FA-2DG-D analyzed by dynamic*
934 *light scattering (DLS) in triplicate. (**C**) (i) Hydrodynamic diameter, and (ii) zeta potential of FA-*
935 *2DG-D-Niclo analyzed by DLS in triplicate.*

936

937 ***Figure 7*. *Characterization of FA-2DG-D-Niclo conjugate and intermediates:*** *(**A**) Table showing*
938 *the physicochemical properties of FA-2DG-D-Niclo and image showing the increase in solubility*
939 *of niclosamide after conjugation with FA-2DG-D scaffold (FA-2DG-D-Niclo). (**B**) The figure*
940 *shows the reproducibility in the synthesis of multiple 400 mg-scale batches of FA-2DG-D-Niclo*
941 *via $^{1}$H NMR and HPLC. The $^{1}$H NMR spectra of 3 batches (400 mg scale) show characteristic*
942 *protons from FA-2DG-D-Niclo. The HPLC chromatographs show reproducibility in the purity of*
943 *these batches with all these batches showing >99% purity. (**C**) In vitro drug release profile of FA-*
944 *2DG-D-Niclo conjugate in PBS and 0.1mM GSH, intracellular conditions at 37$^{o}$C after 15 days,*
945 *and in (100%) human plasma after 120 hours.*

946

947 ***Figure 8*. *Quantitative analysis of FRβ$^{+}$ cells in the lesion and peritoneum following dendrimer***
948 ***treatments.*** *(**A**) Study design as described in Methods. (**B**) Representative immunohistochemical*
949 *images (left) and quantification of FRβ$^{+}$ cells (right) in lesions at 14 or 21 days after lesion*
950 *induction (n=3-8, as dendrimer-Niclo inhibited lesion development). One-way ANOVA followed*
951 *by the Tukey multiple-comparison test was used to assess differences among groups. **(C)***
952 *Representative flow plots (left) and quantification of peritoneal FRβ$^{+}$ cells (right). Differences in*
953 *peritoneal FRβ$^{+}$ cells among groups at each time point were assessed by the Kruskal-Wallis test.*
954 *Data in all figures are shown as the mean ± SEM (n=8). $p < 0.05$ (*), or $p < 0.01$ (**).*

955 ***Figure 9*. *Efficacy of FA-2DG-D-Niclo on treating endometriosis.*** *(A) Quantification of lesion*
956 *numbers and volumes in mice at Days 14 and 21 after lesion induction. Lesion volumes were*
957 *calculated as length × width*$^2$*. Differences in lesion number and volume among groups at each*
958 *time point were assessed by the Kruskal-Wallis test. (**B**) Evaluation of endometriosis-associated*
959 *hyperalgesia. Abdominal (left) and hindpaw (right) withdrawal thresholds were assessed by the*
960 *von Frey test. Data represent the group mean threshold at the corresponding time point (n=16 at*
961 *Day -1 and Day 7, n=8 at Day 14 and Day 21). Red arrows show the time of i.p. administration*
962 *of FA-2DG-D or FA-2DG-D-Niclo. The time course differences within each treatment group*
963 *were compared using a Kruskal-Wallis test followed by the Dunnett multiple-comparison test.*
964 *The colored stars or ns (non-significance) represent the differences at the corresponding time*
965 *point relative to Day -1 within the treatment group. To compare dosing effects of niclosamide at*
966 *each time point among groups, the Kruskal-Wallis test was used. Data are shown as mean ±*
967 *SEM (n=8).* $p < 0.05$ *(*), * $p < 0.01$ *(**), * $p < 0.001$ *(***), or * $p < 0.0001$ *(****).*

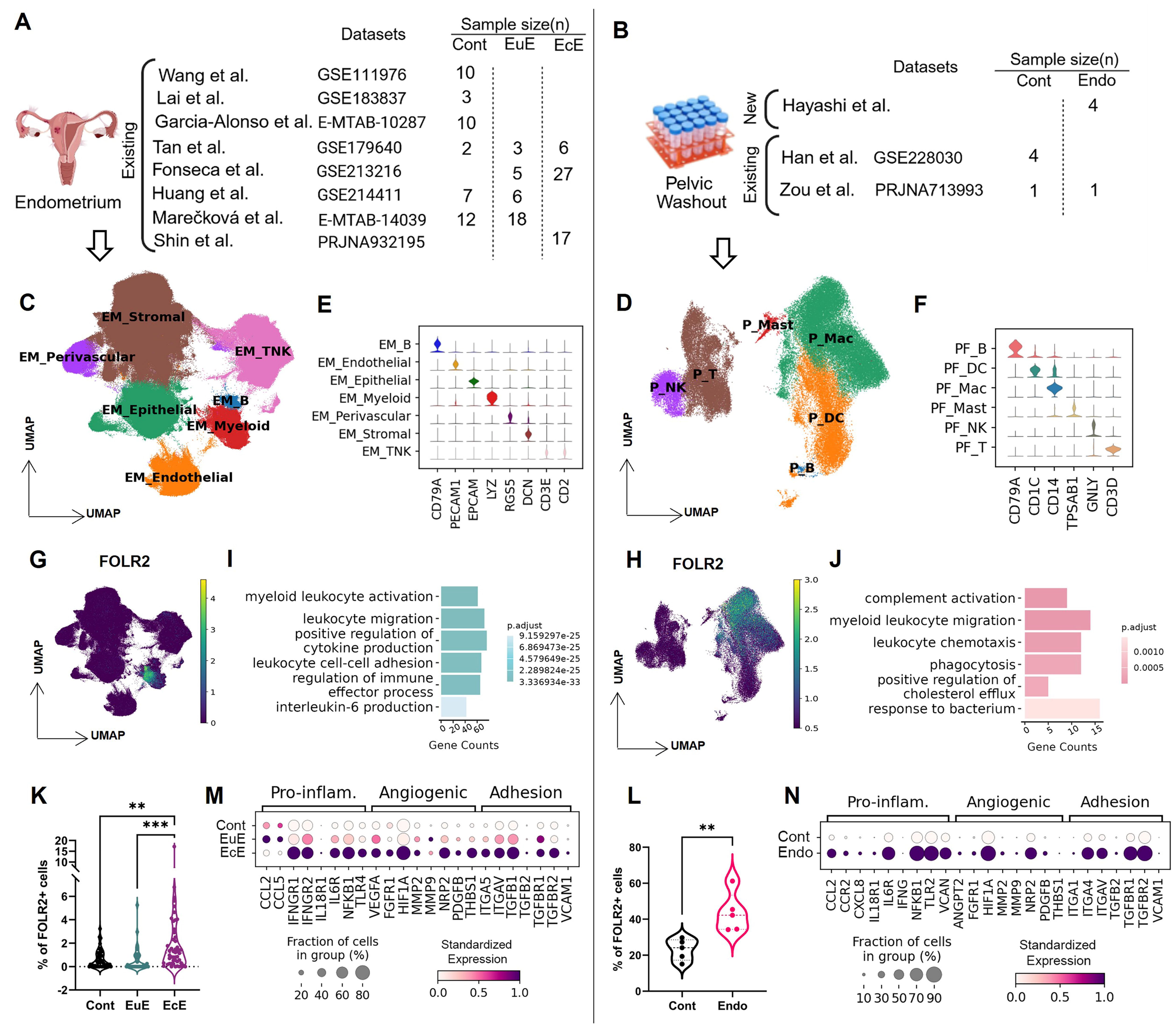
A
Datasets
Sample size(n)
Cont
EuE
EcE
Existing
Wang et al. GSE111976 10
Lai et al. GSE183837 3
Garcia-Alonso et al. E-MTAB-10287 10
Tan et al. GSE179640 2 3 6
Fonseca et al. GSE213216 5 27
Huang et al. GSE214411 7 6
Marečková et al. E-MTAB-14039 12 18
Shin et al. PRJNA932195 17
Endometrium
B
Datasets
Sample size(n)
Cont
Endo
New
Hayashi et al. 4
Existing
Han et al. GSE228030 4
Zou et al. PRJNA713993 1 1
Pelvic Washout
C
EM_Stromal
EM_Perivascular
EM_TNK
EM_Epithelial
EM_B
EM_Myeloid
EM_Endothelial
UMAP
UMAP
D
P_Mast
P_Mac
P_T
P_NK
P_DC
P_B
UMAP
UMAP
E
EM_B
EM_Endothelial
EM_Epithelial
EM_Myeloid
EM_Perivascular
EM_Stromal
EM_TNK
CD79A
PECAM1
EPCAM
LYZ
RGS5
DCN
CD3E
CD2
F
PF_B
PF_DC
PF_Mac
PF_Mast
PF_NK
PF_T
CD79A
CD1C
CD14
TPSAB1
GNLY
CD3D
G
FOLR2
UMAP
UMAP
H
FOLR2
UMAP
UMAP
I
myeloid leukocyte activation
leukocyte migration
positive regulation of cytokine production
leukocyte cell-cell adhesion
regulation of immune effector process
interleukin-6 production
p.adjust
9.159297e-25
6.869473e-25
4.579649e-25
2.289824e-25
3.336934e-33
Gene Counts
J
complement activation
myeloid leukocyte migration
leukocyte chemotaxis
phagocytosis
positive regulation of cholesterol efflux
response to bacterium
p.adjust
0.0010
0.0005
Gene Counts
K
% of FOLR2+ cells
Cont
EuE
EcE
L
% of FOLR2+ cells
Cont
Endo
M
Pro-inflam.
Angiogenic
Adhesion
Cont
EuE
EcE
CCL2
CCL5
IFNGR1
IFNGR2
IL18R1
IL6R
NFKB1
TLR4
VEGFA
FGFR1
HIF1A
MMP2
MMP9
NRP2
PDGFB
THBS1
ITGA5
ITGAV
TGFB1
TGFB2
TGFBR1
TGFBR2
VCAM1
Fraction of cells in group (%)
Standardized Expression
N
Pro-inflam.
Angiogenic
Adhesion
Cont
Endo
CCL2
CCR2
CXCL8
IL18R1
IL6R
IFNG
NFKB1
TLR2
VCAN
ANGPT2
FGFR1
HIF1A
MMP2
MMP9
NRP2
PDGFB
THBS1
ITGA1
ITGA4
ITGAV
TGFB2
TGFBR1
TGFBR2
VCAM1
Fraction of cells in group (%)
Standardized Expression

## A. Synthesis of FA-2DG-D-Cy5

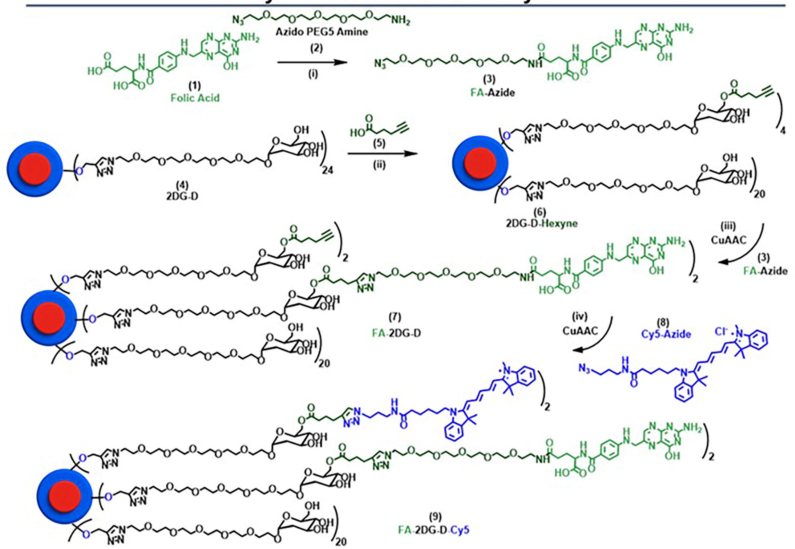


## B. $^1$H NMR Characterization of FA-2DG-D-Cy5

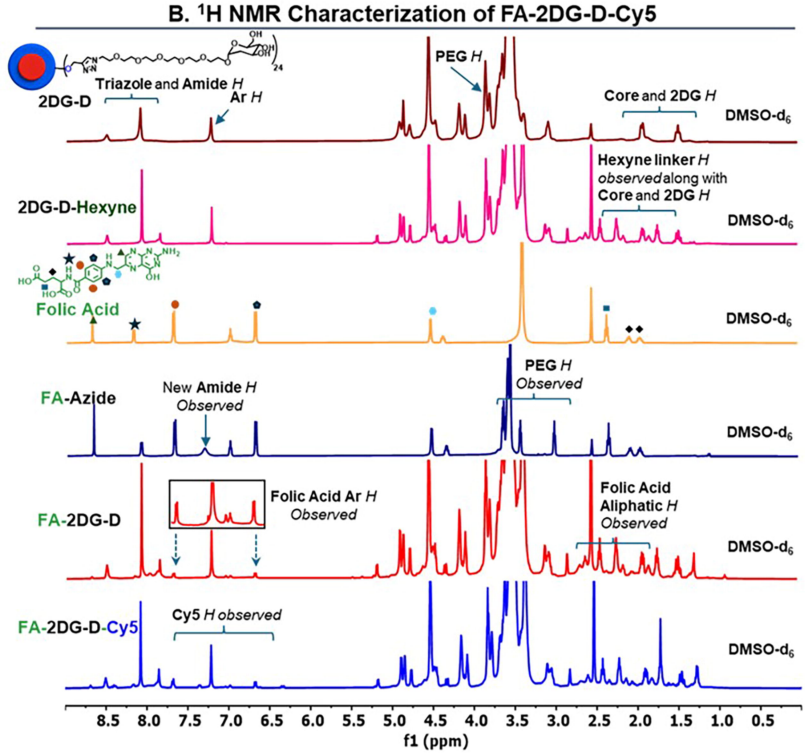

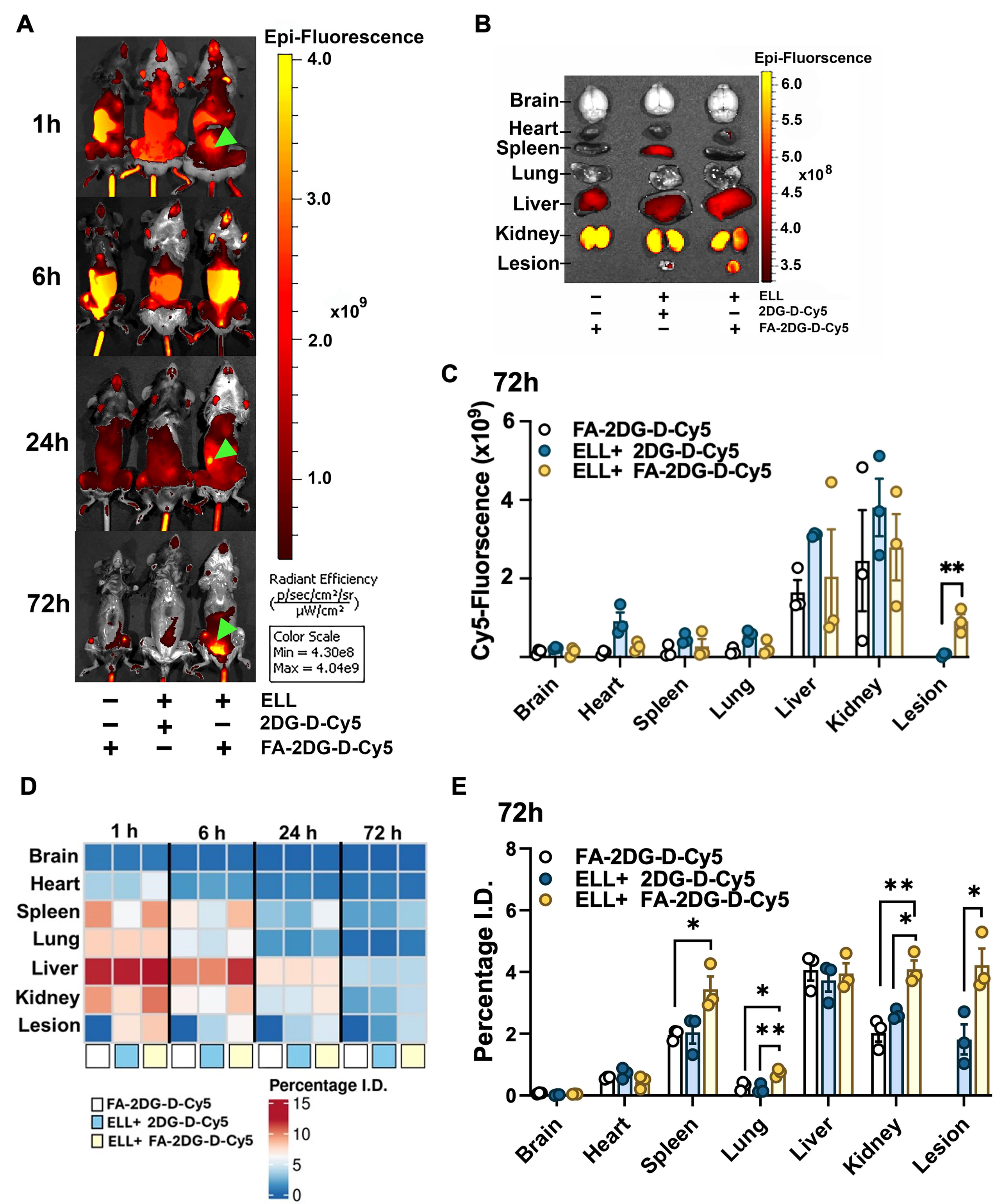
A
Epi-Fluorescence
4.0
3.0
2.0
1.0
x10^9
1h
6h
24h
72h
Radiant Efficiency
(p/sec/cm²/sr / µW/cm²)
Color Scale
Min = 4.30e8
Max = 4.04e9
− + + ELL
− + − 2DG-D-Cy5
+ − + FA-2DG-D-Cy5
B
Epi-Fluorscence
Brain
Heart
Spleen
Lung
Liver
Kidney
Lesion
6.0
5.5
5.0
x10^8
4.5
4.0
3.5
− + + ELL
− + − 2DG-D-Cy5
+ − + FA-2DG-D-Cy5
C
72h
Cy5-Fluorscence (x10^9)
FA-2DG-D-Cy5
ELL+ 2DG-D-Cy5
ELL+ FA-2DG-D-Cy5
**
Brain
Heart
Spleen
Lung
Liver
Kidney
Lesion
D
1 h
6 h
24 h
72 h
Brain
Heart
Spleen
Lung
Liver
Kidney
Lesion
FA-2DG-D-Cy5
ELL+ 2DG-D-Cy5
ELL+ FA-2DG-D-Cy5
Percentage I.D.
15
10
5
0
E
72h
Percentage I.D.
FA-2DG-D-Cy5
ELL+ 2DG-D-Cy5
ELL+ FA-2DG-D-Cy5
*
*
**
**
*
Brain
Heart
Spleen
Lung
Liver
Kidney
Lesion

## A. Peritoneal cells

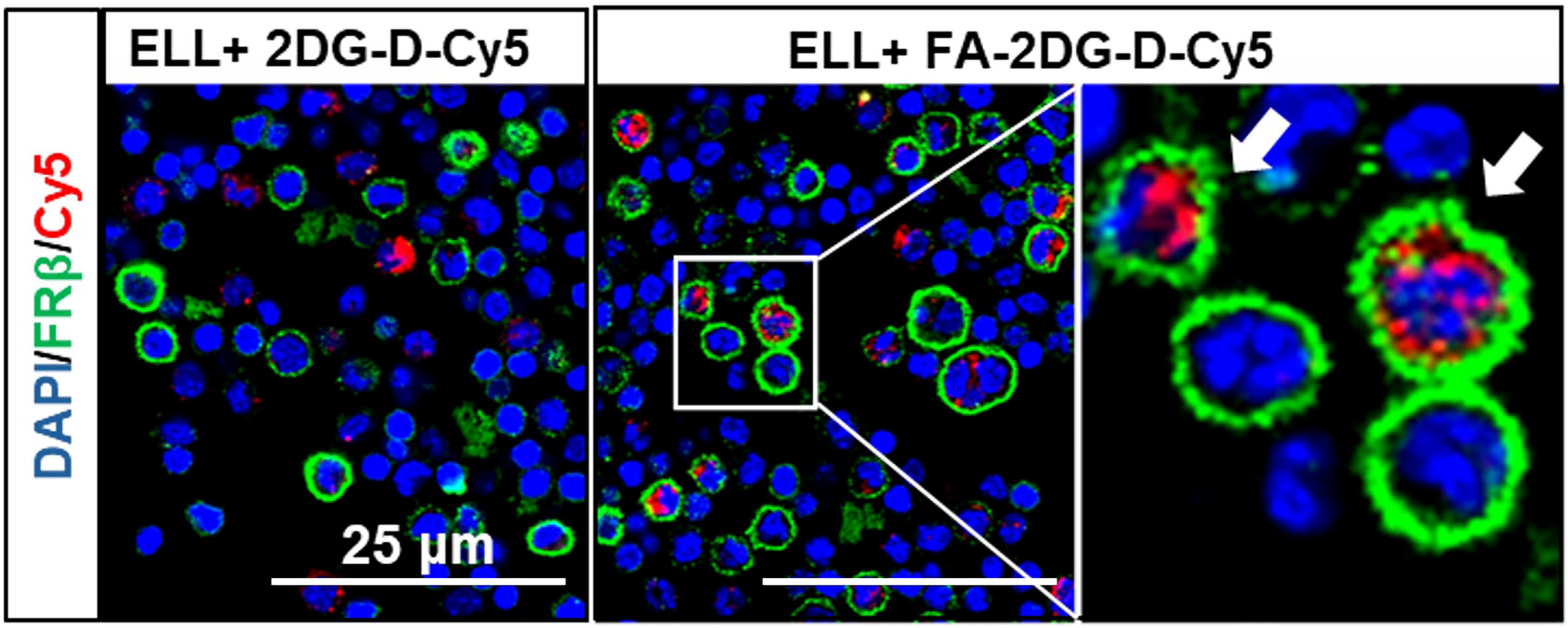


## B. Lesions

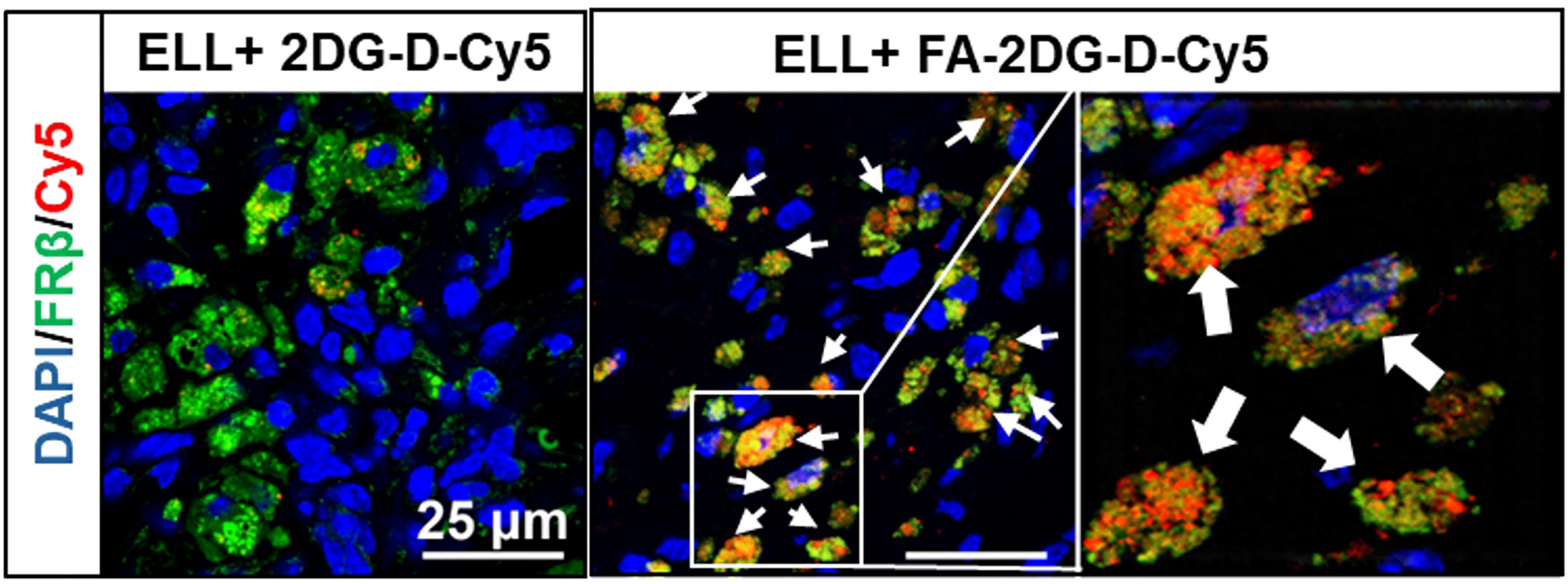


## C. Major organs

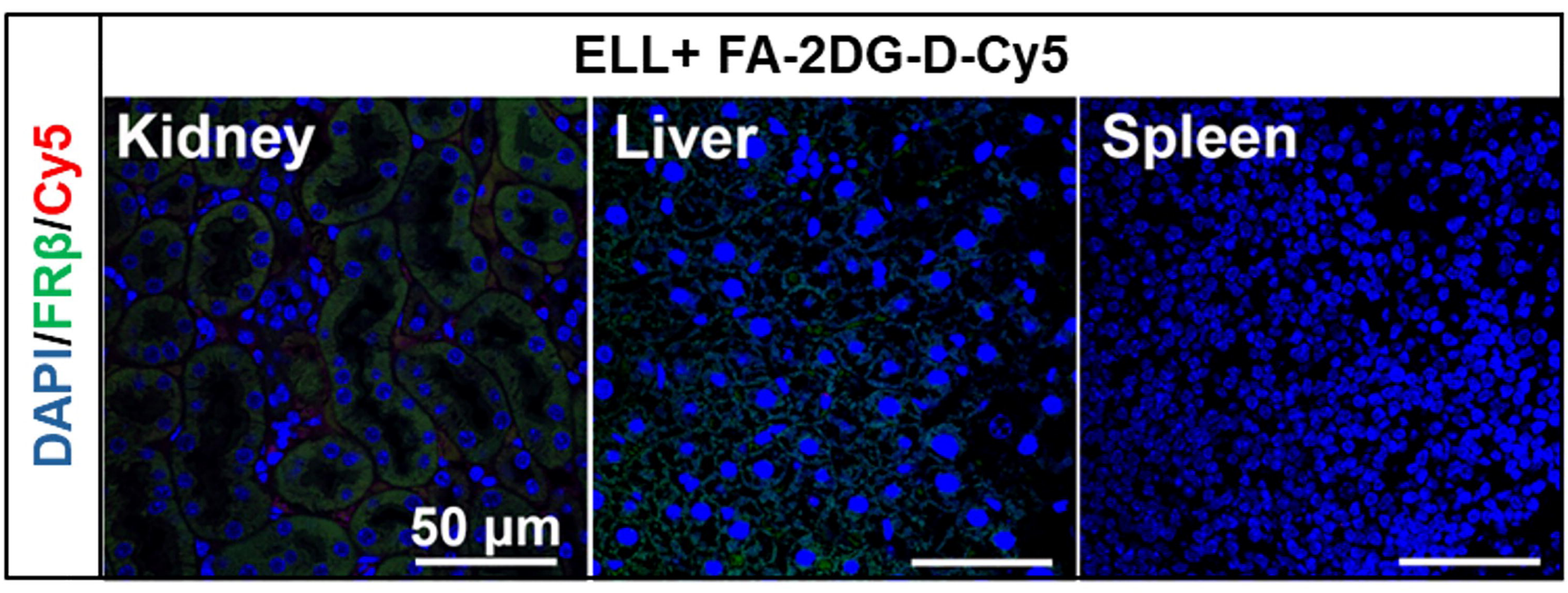

## A. Synthesis of FA-2DG-D-Niclo

### (i) Synthesis of Niclo-Azide

### (ii) Synthesis of FA-2DG-D-Niclo

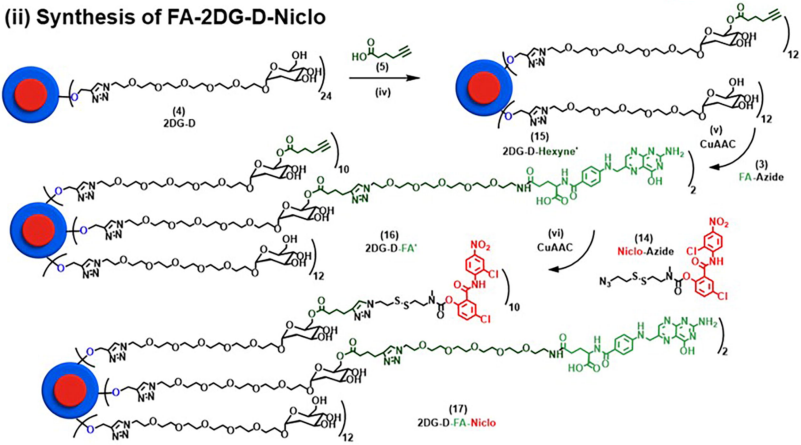


## B. $^1$H NMR Characterization of FA-2DG-D-Niclo

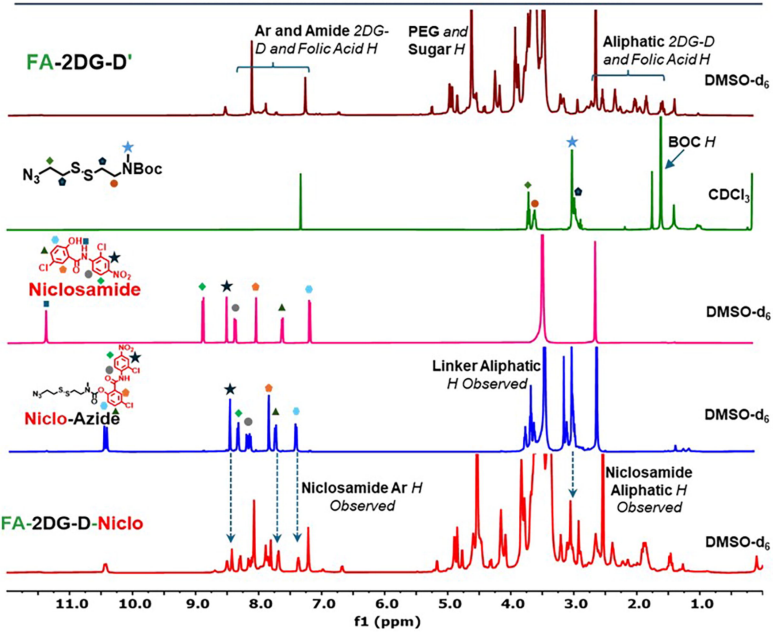

## A. HPLC Characterization of FA-2DG-D-Niclo

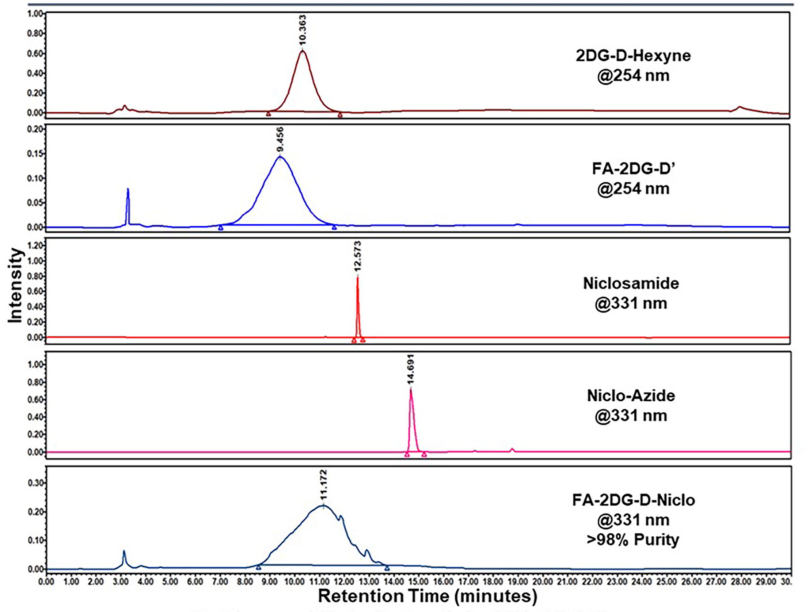


## B. Size and Zeta Potential of FA-2DG-D

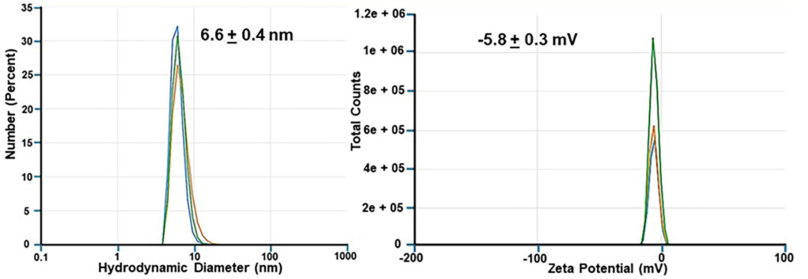


## C. Size and Zeta Potential of FA-2DG-D-Niclo

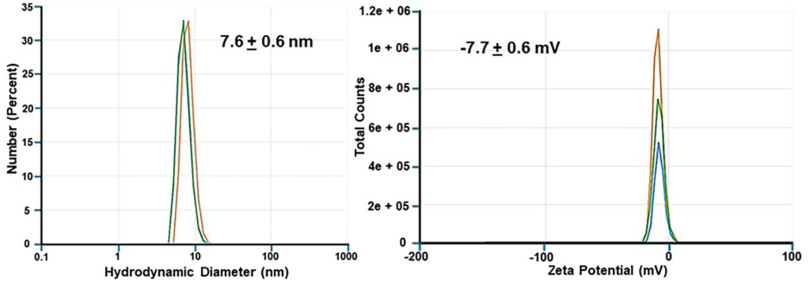

## A. Physicochemical Properties and Solubility of FA-2DG-D-Niclo

| Physicochemical Properties of FA-2DG-D-Niclo | |
|---|---|
| Hydrodynamic Diameter | 7.6 ± 0.6 nm |
| Zeta Potential | -7.7 ± 0.6 mV |
| HPLC Purity | >98% |
| Drug Loading | ~12% |
| Solubility | 150 mg/mL |

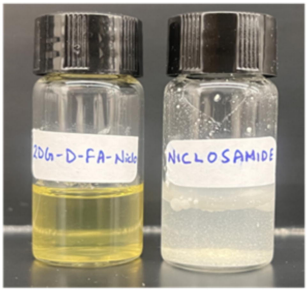


1. FA-2DG-D-Niclo at 18 mg/mL (Niclosamide equivalent concentration)
2. Niclosamide at 1 mg/mL

## B. Reproducible Synthesis of FA-2DG-D-Niclo

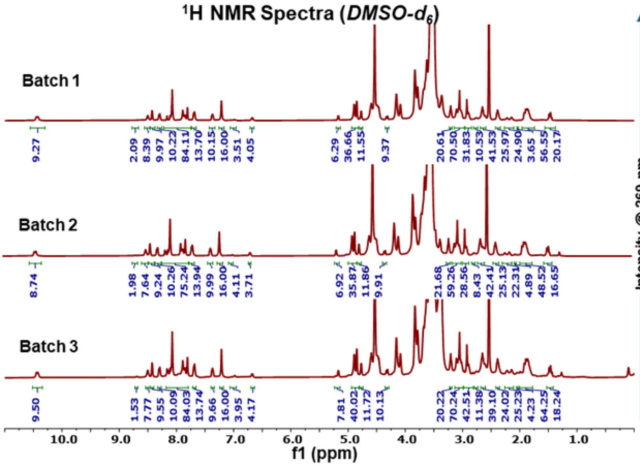


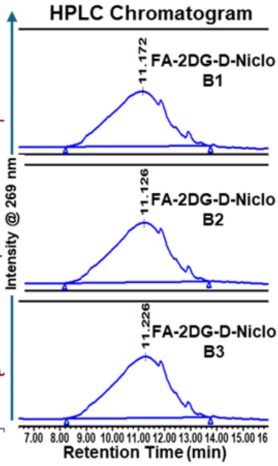


## C. *In Vitro* Drug Release Profile of FA-2DG-D-Niclo

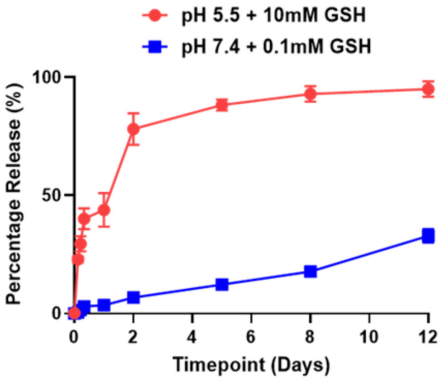


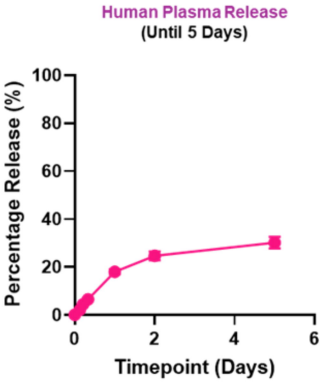

A

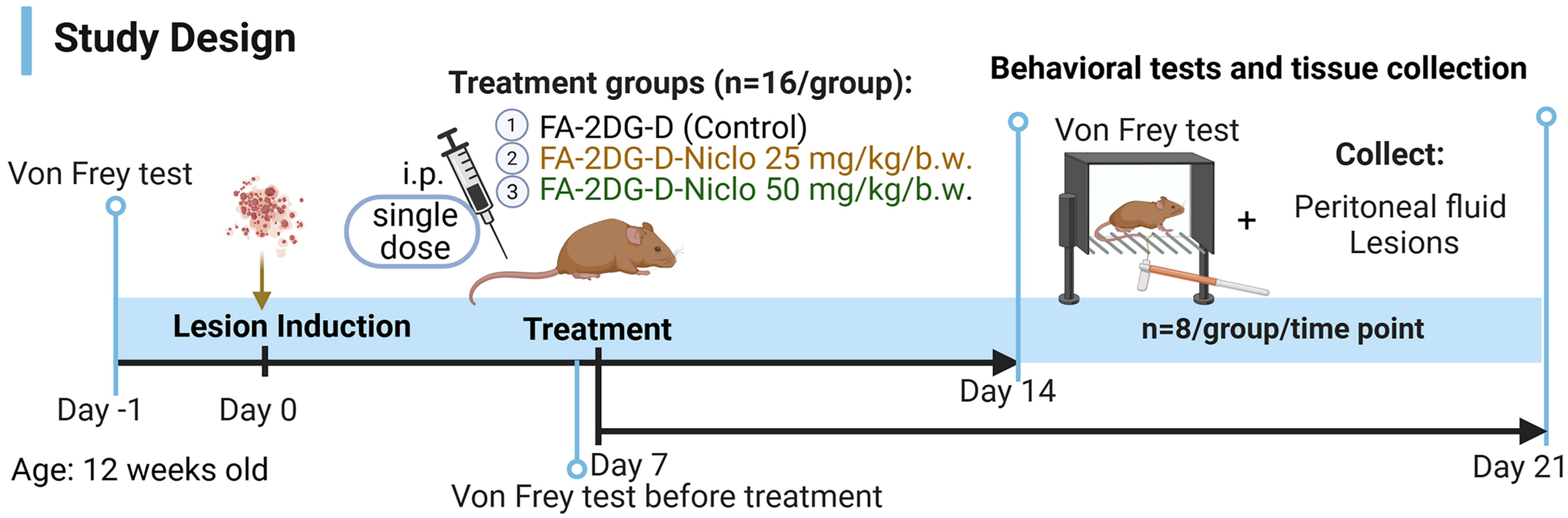
Study Design
Treatment groups (n=16/group):
1 FA-2DG-D (Control)
2 FA-2DG-D-Niclo 25 mg/kg/b.w.
3 FA-2DG-D-Niclo 50 mg/kg/b.w.
Behavioral tests and tissue collection
Von Frey test
i.p.
single dose
Von Frey test
Collect:
Peritoneal fluid
Lesions
+
Lesion Induction
Treatment
n=8/group/time point
Day -1
Day 0
Day 14
Age: 12 weeks old
Day 7
Von Frey test before treatment
Day 21

B

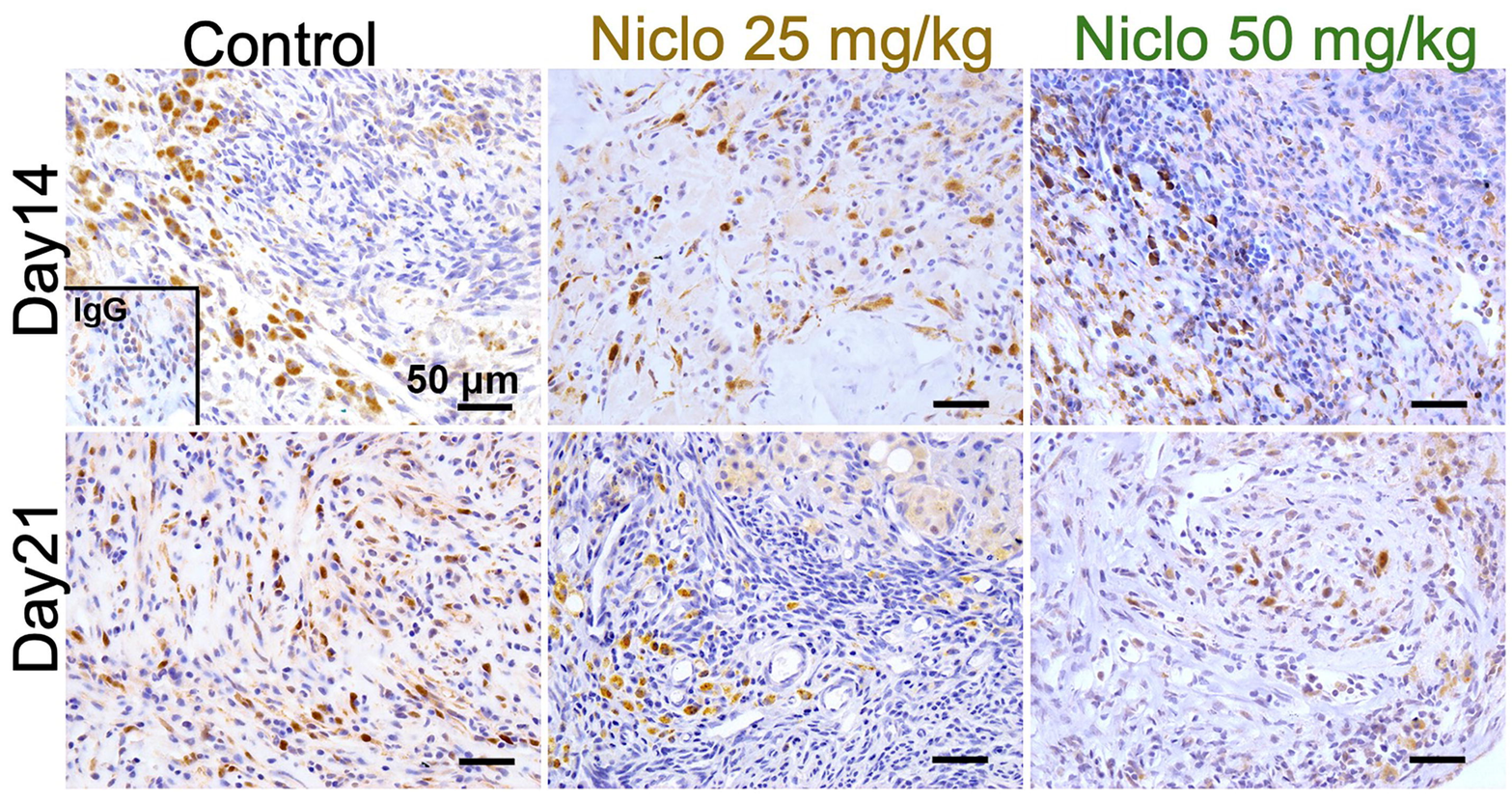
Control
Niclo 25 mg/kg
Niclo 50 mg/kg
Day14
Day21
IgG
50 µm

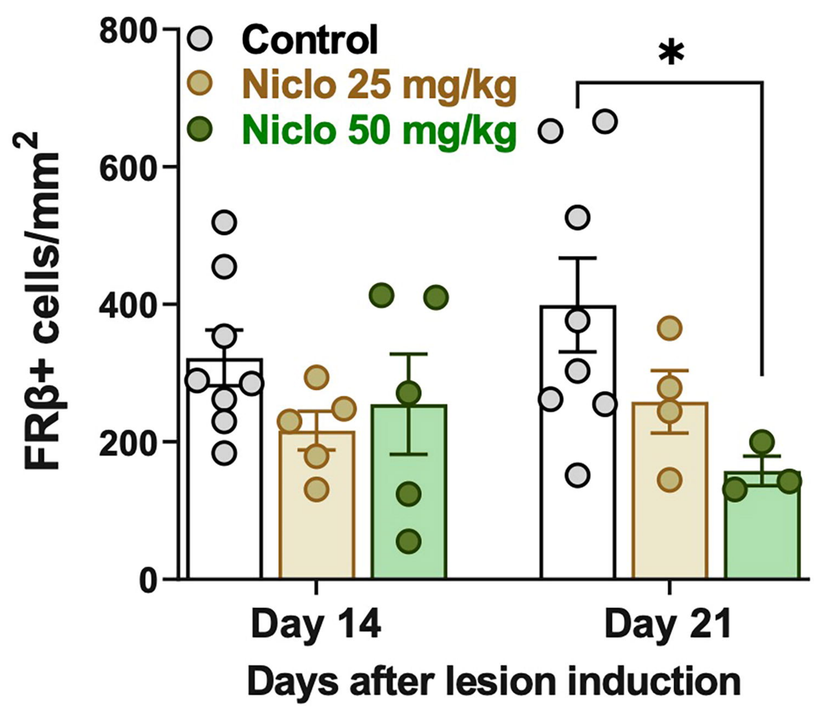
Control
Niclo 25 mg/kg
Niclo 50 mg/kg
FRβ+ cells/mm2
800
600
400
200
0
*
Day 14
Day 21
Days after lesion induction

C

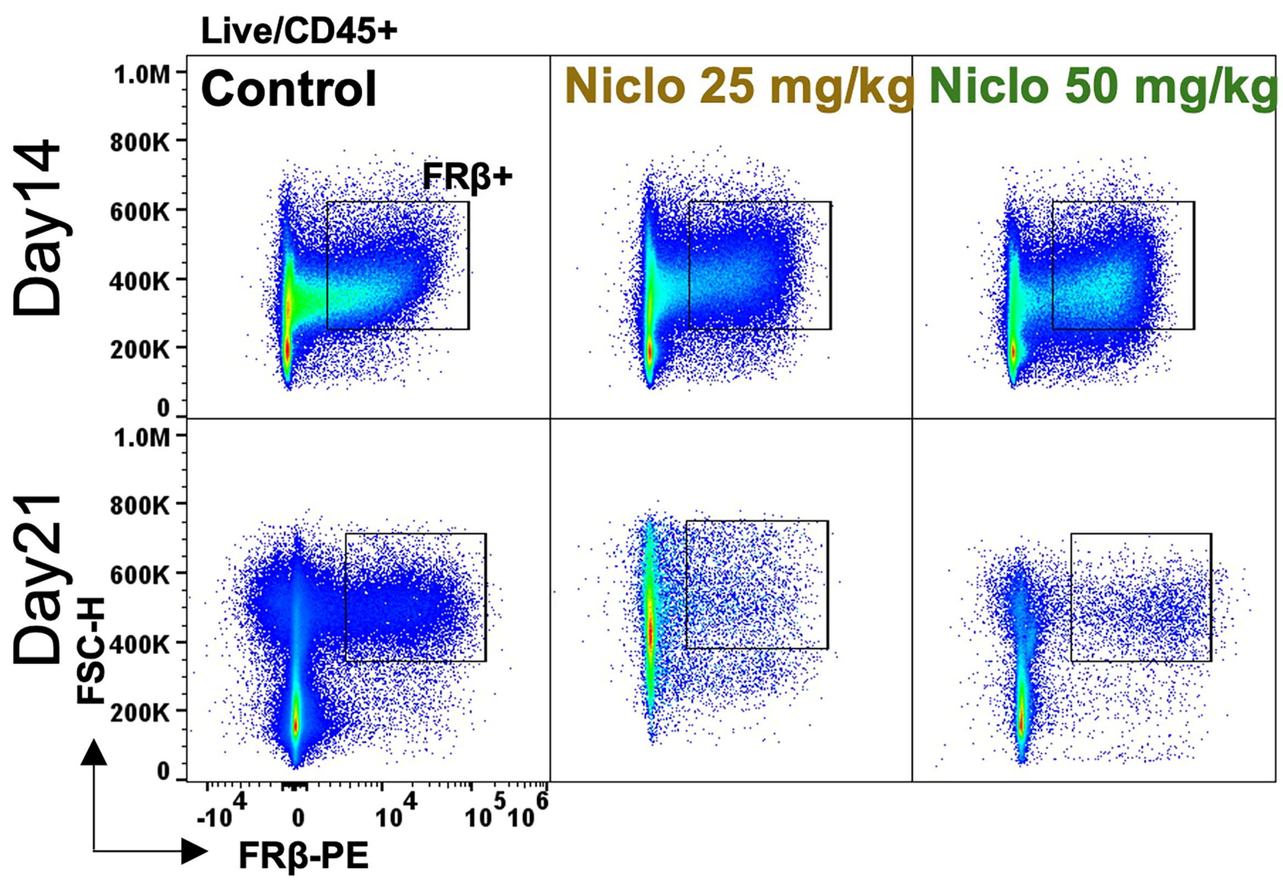
Live/CD45+
Control
Niclo 25 mg/kg
Niclo 50 mg/kg
Day14
Day21
FRβ+
1.0M
800K
600K
400K
200K
0
FSC-H
FRβ-PE

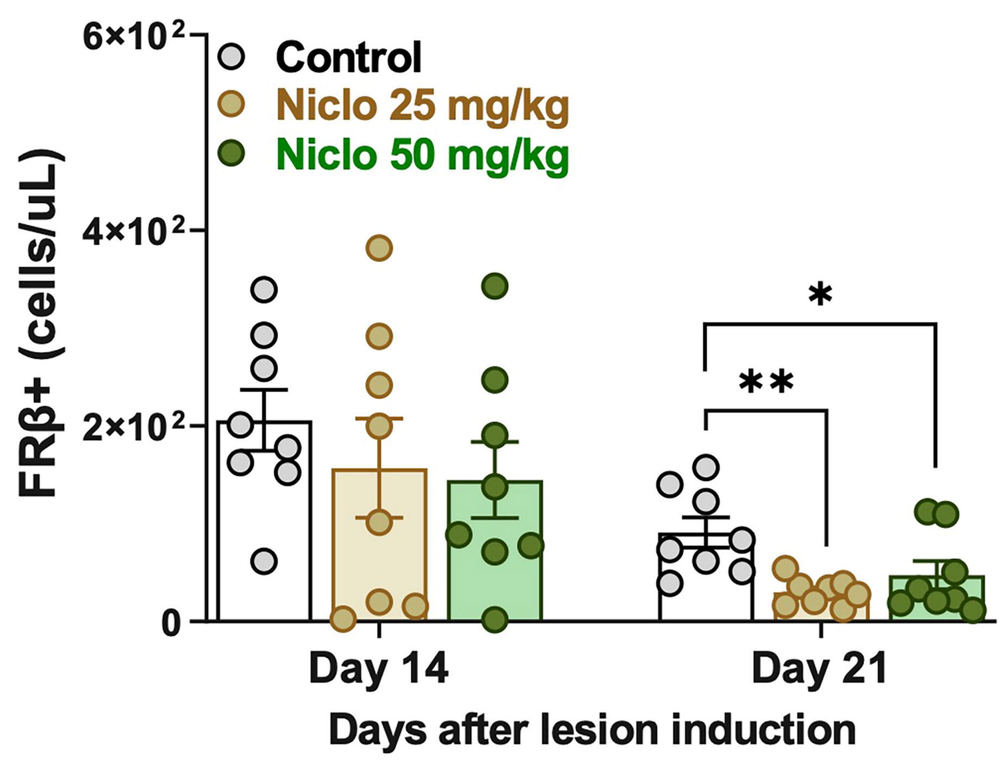
Control
Niclo 25 mg/kg
Niclo 50 mg/kg
FRβ+ (cells/uL)
6×10²
4×10²
2×10²
0
*
**
Day 14
Day 21
Days after lesion induction

A

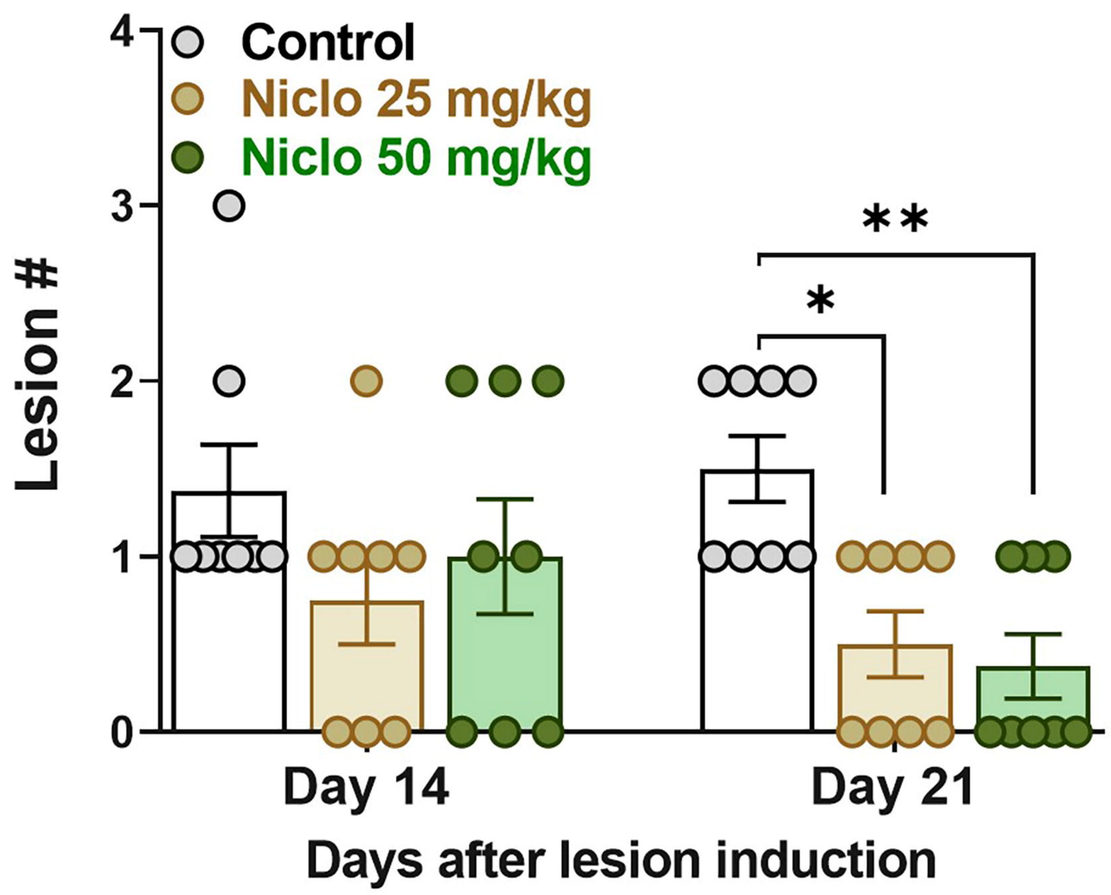
Control
Niclo 25 mg/kg
Niclo 50 mg/kg
Lesion #
4
3
2
1
0
**
*
Day 14
Day 21
Days after lesion induction

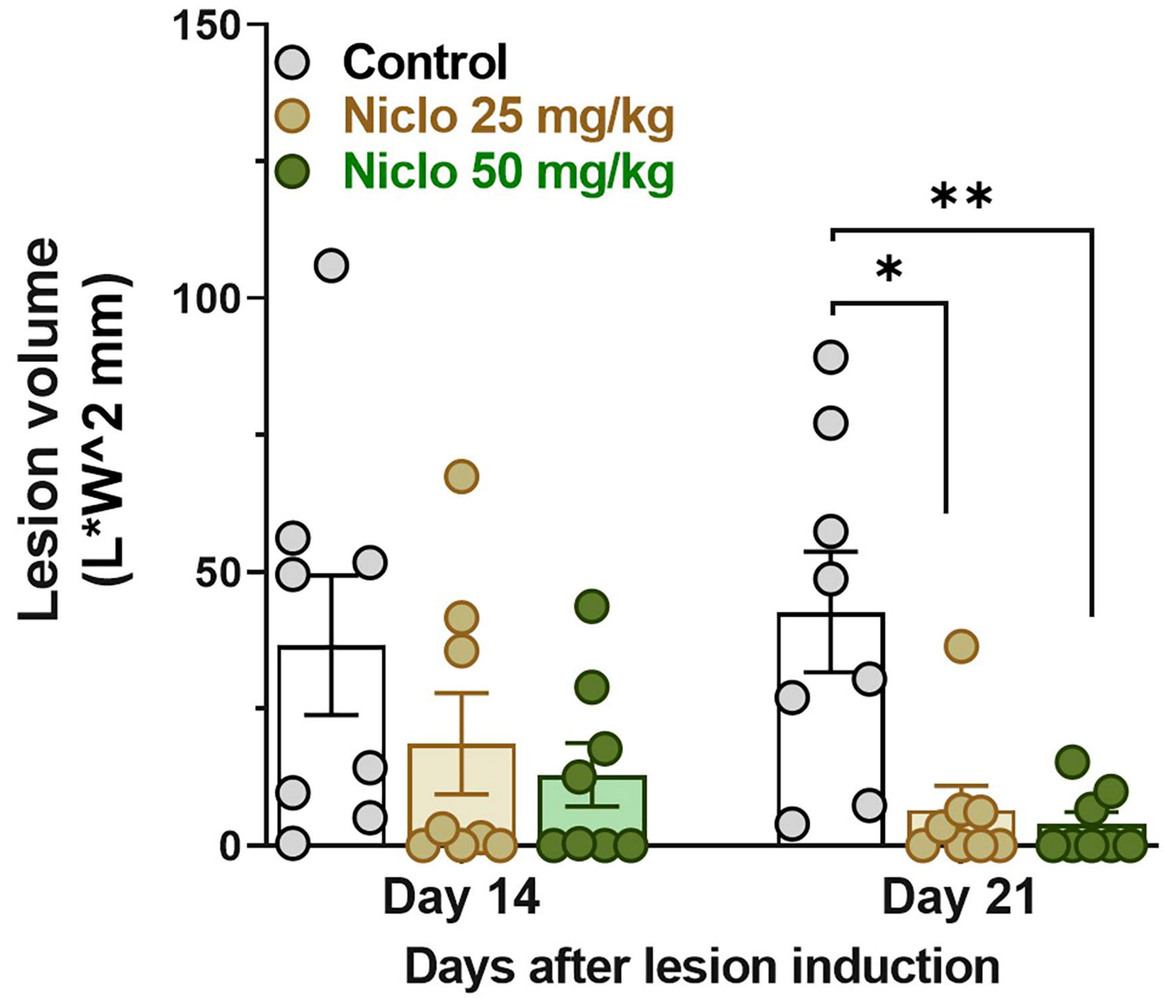
Control
Niclo 25 mg/kg
Niclo 50 mg/kg
Lesion volume
(L*W^2 mm)
150
100
50
0
**
*
Day 14
Day 21
Days after lesion induction

B

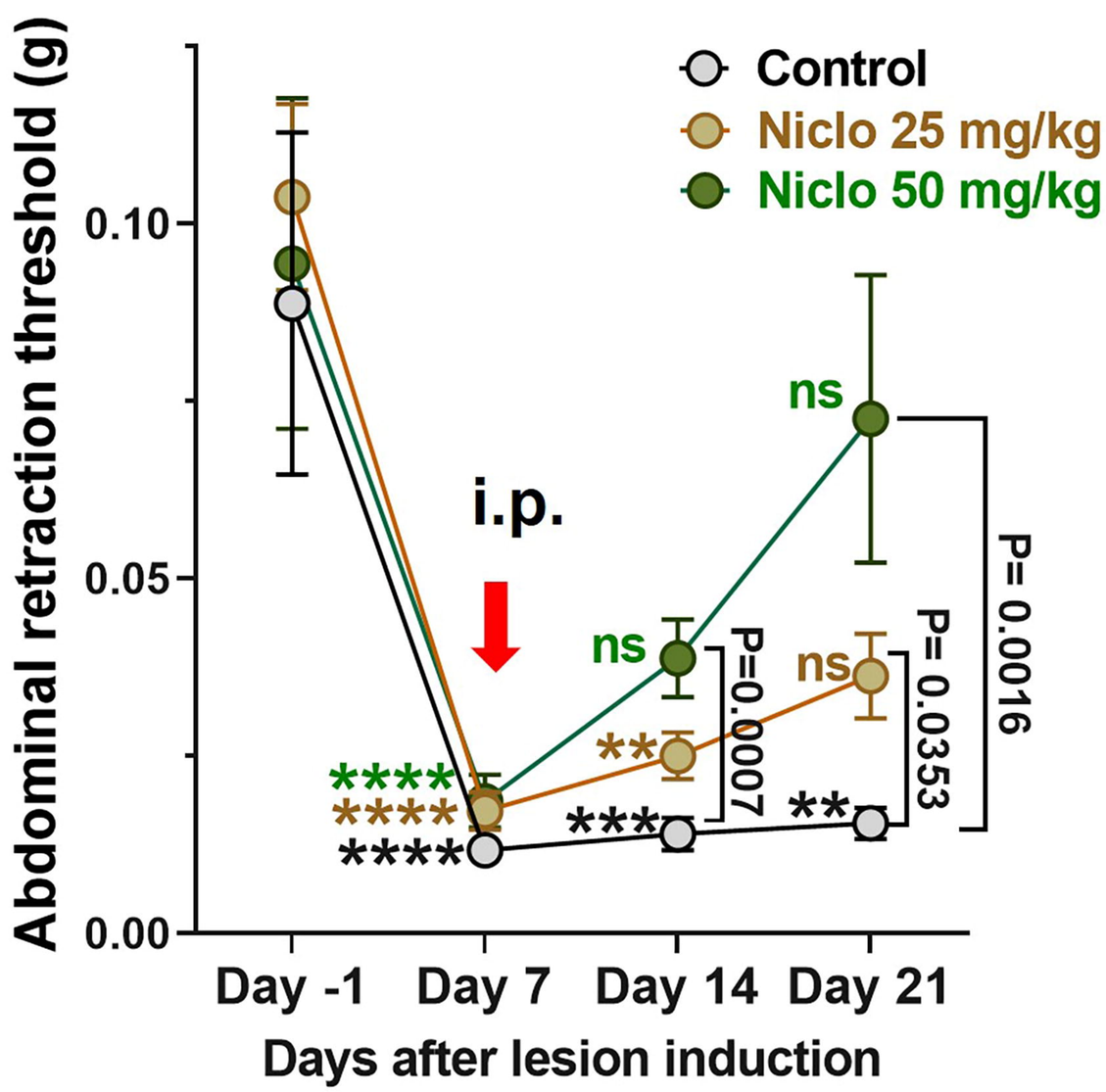
Control
Niclo 25 mg/kg
Niclo 50 mg/kg
Abdominal retraction threshold (g)
0.10
0.05
0.00
i.p.
ns
ns
ns
****
****
****
**
***
**
P=0.0007
P= 0.0353
P= 0.0016
Day -1
Day 7
Day 14
Day 21
Days after lesion induction

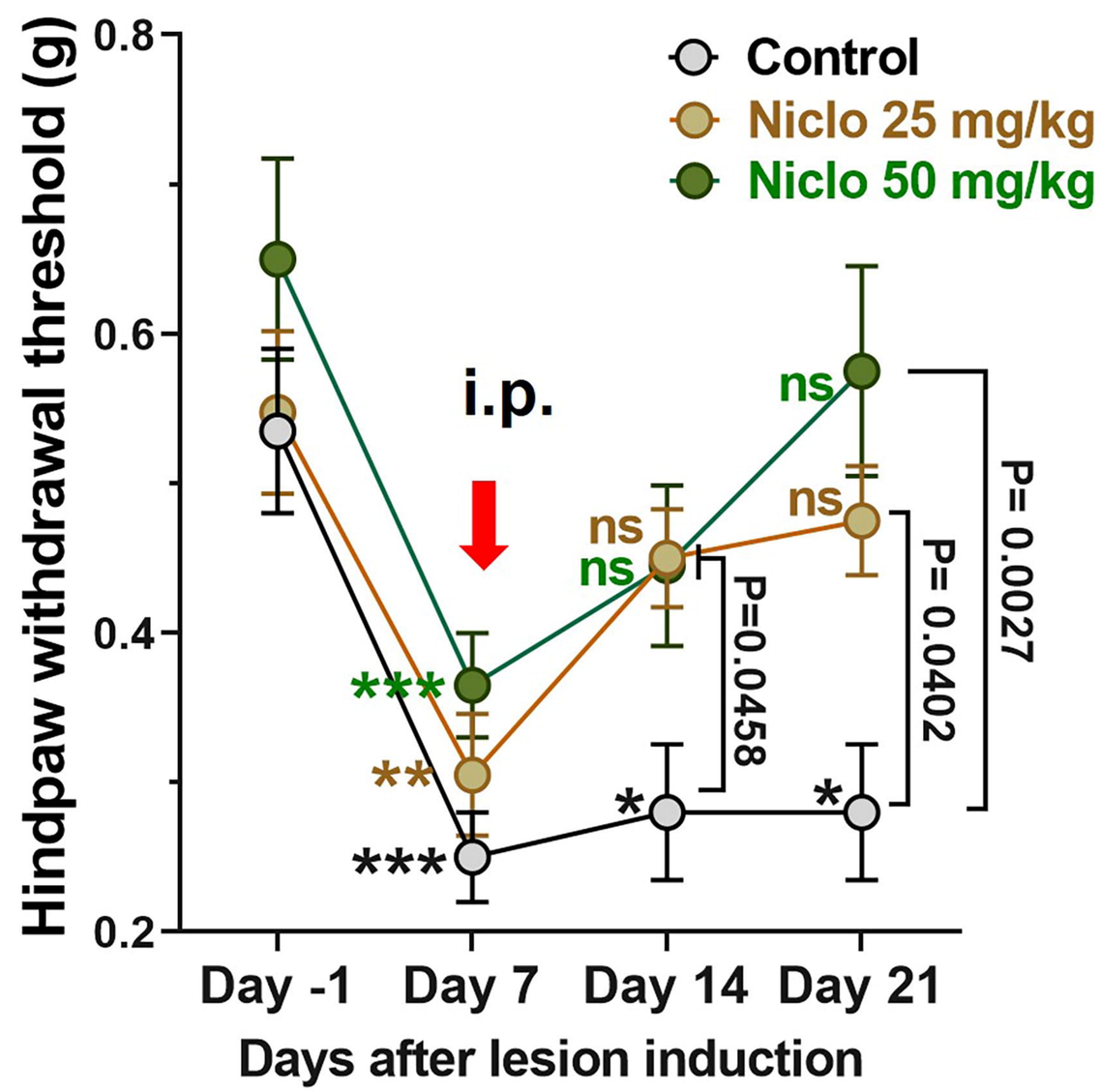
Control
Niclo 25 mg/kg
Niclo 50 mg/kg
Hindpaw withdrawal threshold (g)
0.8
0.6
0.4
0.2
i.p.
ns
ns
ns
ns
***
**
***
*
*
P=0.0458
P= 0.0402
P= 0.0027
Day -1
Day 7
Day 14
Day 21
Days after lesion induction